Improving Convection-Allowing Ensemble Forecasts by Assimilating Radar Reflectivity and FY Satellite TBB/Total Cloud Water Through Stepwise Cloud-Analysis Initialization: A Remote Sensing Case Study

Guo Deng , Xiefei Zhi * , Lijuan Zhu , Yushu Zhou , Fajing Chen , Kaiyan Wu , Jing Chen , Hongqi Li ,
Jingzhuo Wang , Jian Yue , Zhizhen Xu

Posted Date: 18 May 2026

doi: 10.20944/preprints202605.1096.v1

Keywords: cloud analysis; radar reflectivity; FY-2G remote sensing data; hydrometeor initialization; convective-scale ensemble forecasting

doi:10.20944/preprints202605.1096.v1

Article

Improving Convection-Allowing Ensemble Forecasts by Assimilating Radar Reflectivity and FY Satellite TBB/Total Cloud Water Through Stepwise Cloud-Analysis Initialization: A Remote Sensing Case Study

Guo Deng [1,2,3], Xiefei Zhi [4,5]*, Lijuan Zhu [1,2], Yushu Zhou [6,7], Fajing Chen [1,2], Kaiyan Wu [8], Jing Chen [1,2], Hongqi Li [1,2], Jingzhuo Wang [1,2], Jian Yue [1,2] and Zhizhen Xu [1,2]

[1] CMA Earth System Modeling and Prediction Centre (CEMC),Beijing100081,China
[2] State Key Laboratory of Severe Weather Meteorological Science and Technology (LaSW), Beijing100081, China
[3] National Meteorological Centre,CMA,Beijing100081,China
[4] Key Laboratory of Meteorology Disaster, Ministry of Education, Nanjing University of Information Science and Technology, Nanjing, China
[5] Stellerus Technology Co. Ltd., Hong Kong, China
[6] Laboratory of Cloud-Precipitation Physics and Severe Storms, Institute of Atmospheric Physics, Chinese Academy of Sciences, Beijing 100029, China
[7] University of Chinese Academy of Science, Beijing 100049, China
[8] Chinese Academy of Meteorological Sciences (CAMS), Beijing100081,China
* Correspondence: zhi@nuist.edu.cn

Highlights

What are the main findings?

- Within a convective-scale ensemble forecasting system, a nudging-based cloud analysis scheme is implemented to assimilate multi-source remote sensing data—including three-dimensional mosaic radar reflectivity, hourly averaged FY-2G satellite black-body temperature (TBB), and FY-2G total cloud water products—to generate three-dimensional hydrometeor increments for each ensemble member. This remote sensing-driven approach proves highly suitable for introducing cloud information into convection-permitting models, enabling smooth coordination between hydrometeor fields and the model's dynamic-thermal framework without inducing spin-up shock.
- The incorporation of radar- and satellite-derived hydrometeor information significantly enhances the convective-scale ensemble prediction system's overall performance. Model spin-up time is markedly reduced as the slow condensation process from water vapor is bypassed by directly initializing cloud fields from remote sensing retrievals, leading to systematic improvements in both deterministic and probabilistic forecasts for temperature, wind, geopotential height, and precipitation—with benefits sustained throughout the 12-48-hour forecast range.

What are the implications of the main findings?

- The enhanced ensemble forecast skill is driven by multiple physical mechanisms triggered within the convective-scale modeling framework by the assimilated remote sensing data: (i) shortened spin-up accelerates the establishment of realistic cloud-precipitation microphysics, thanks to the realistic hydrometeor distribution provided by radar reflectivity and satellite TBB/cloud water; (ii) latent heat release from rapidly formed clouds directly warms the mid-troposphere, adjusting 500 hPa thermal-dynamic structures and correcting systematic biases;

(iii) cloud-radiation interactions—informed by satellite-observed cloud properties—further refine vertical temperature profiles, collectively improving the representation of convective processes.

- This study demonstrates that incorporating remote sensing-based cloud analysis via nudging offers a computationally efficient pathway to address a long-standing challenge in convective-scale ensemble systems—the lack of hydrometeor information in initial conditions. By providing ensemble members with physically coordinated initial fields that integrate radar and FY-2G satellite observations with thermal, dynamic, and microphysical consistency, this approach substantially improves short-term ensemble forecasting capability and establishes a practical benchmark for future assimilation developments targeting convection-permitting models.

Abstract

The “spin-up” problem—where convection-permitting models require hours to develop realistic clouds from large-scale initial fields—critically limits short-term severe weather forecasting. Cloud analysis offers a potential solution by directly incorporating hydrometeor information from remote sensing observations. In this study, we leverage multi-source remote sensing data, including three-dimensional mosaic radar reflectivity, hourly averaged FY-2G satellite black-body temperature (TBB), and FY-2G total cloud water products, within a stepwise cloud-analysis initialization scheme. The scheme is implemented in a convective-scale ensemble forecasting system (CMA-Meso, 3 km resolution) for a heavy rainfall event. For each ensemble member, three-dimensional hydrometeor increments are independently generated from these remote sensing retrievals and gradually introduced over the first ten time steps, ensuring smooth coordination with the model’s dynamic-thermal framework. Results demonstrate that the remote sensing-driven cloud analysis substantially enhances ensemble system performance across multiple dimensions: (i) spin-up time is significantly reduced, with precipitation forecasts exhibiting reasonable structure from the initial forecast hour; (ii) deterministic forecast accuracy improves systematically, with reduced RMSE for geopotential height, temperature, and wind fields across all levels; (iii) probabilistic forecasting skill is enhanced, evidenced by improved CRPS and AROC for surface elements and precipitation thresholds; (iv) ensemble reliability is optimized, with spread better matching forecast errors. Mechanistic analysis reveals that these improvements stem from physically coordinated hydrometeor-latent heat initial perturbations and subsequent cloud-radiation feedbacks that continuously regulate thermal-dynamic structures. This study establishes that assimilating diverse remote sensing data via cloud analysis is an effective approach for addressing spin-up challenges in convective-scale ensemble prediction.

Keywords: cloud analysis; radar reflectivity; FY-2G remote sensing data; hydrometeor initialization; convective-scale ensemble forecasting

1. Introduction

China experiences frequent severe convective weather, with the disasters it triggers ranking among the primary meteorological hazards (Zhou et al., 2025). Characterized by small spatial scales, short lifecycles, high suddenness, and rapid development, severe convective weather poses significant challenges in operational weather forecasting (Wilson & Roberts, 2006; Jiang et al., 2019). Due to the complexity of atmospheric systems and the lack of observations and analytical challenges regarding mesoscale and small-scale features, significant uncertainties exist in the initial conditions of convective-scale numerical weather prediction, directly affecting forecast accuracy and reliability (Stensrud et al., 2009).With advances in computational power, convective-scale ensemble forecasting models with horizontal resolutions of 2–4 kilometers have become essential operational and research tools. These models aim to enhance short-range (1–3 day) forecasting skills for severe weather events like heavy precipitation by characterizing uncertainties in local details of weather systems (Chen et al., 2025; Johnson, 2025).

However, convective-scale forecasting has long been constrained by the "spin-up" problem (Phillips, 1960). Model initial fields typically lack or contain inaccurate cloud and precipitation particle information, requiring several hours of integration to generate cloud-precipitation systems consistent with the dynamic and thermal fields (Xue et al., 2003). This not only leads to poor short-term forecasting skills (0–6 hours) but also generates inconsistent latent heat release that may influence subsequent circulation evolution, causing forecast biases for high-impact weather events like locally intense convection. To mitigate this issue, assimilating remote sensing observations that directly reflect cloud and precipitation structure has proven effective. In particular, weather radar reflectivity (e.g., three-dimensional mosaic products) and geostationary satellite data (such as FY-2G black-body temperature (TBB) and total cloud water) provide high-resolution, continuous information on hydrometeor distribution (Sun & Crook, 1997; Bauer et al., 2007). Cloud analysis systems integrate these multi-source remote sensing data to reconstruct physically consistent three-dimensional cloud and precipitation particle fields, offering models more realistic, moist initial conditions. By "implanting" observed convective systems derived from radar and satellite retrievals into the initial field, these systems significantly reduce spin-up time (Albers, 1996; Zhang et al., 1998; Hu et al., 2006). Extensive research confirms that in deterministic forecasting, cloud analysis based on remote sensing data substantially improves the analysis and short-term forecasting of convective storms (e.g., Hu et al., 2006; Xue et al., 2014; Pan et al., 2016).

Despite the widespread application of cloud analysis within deterministic frameworks, its role and mechanisms in ensemble forecasting have long been overlooked. Existing ensemble forecasting research has primarily focused on improving methods for generating initial perturbations in dynamic and thermodynamic fields such as wind, temperature, pressure, and humidity (e.g., BGM, Toth and Kalnay,1993; ETKF,Wang and Bishop, 2003), while insufficient attention has been given to systematic errors and stochastic uncertainties in initial fields of hydrometeors like cloud water, rainwater, and ice crystals (Zhang et al., 2020). However, the moist convective process is precisely the key physical mechanism that causes rapid error growth and limits forecast skill (Hohenegger & Schär, 2007; Bei & Zhang, 2007). If ensemble members differ only in the large-scale environmental fields but lack reasonable representation of critical convective triggers and the onset of microphysical processes, they will struggle to accurately reflect the uncertainty inherent in convective-scale models, thereby limiting the overall performance of ensemble forecasting systems (Wang et al., 2022; Destouches et al., 2023). Therefore, a critical scientific question arises: How can radar and other satellite remote sensing observations (e.g., FY-2G TBB and total cloud water products, three-dimensional radar reflectivity mosaic) be effectively utilized in convective-scale ensemble forecasting to construct physically coherent hydrometeor initial fields incorporating reasonable uncertainty through cloud analysis techniques, thereby systematically enhancing the skill of short-range probabilistic forecasts? Furthermore, exploring the role, mechanisms, and optimization pathways of hydrometeors within the ensemble forecasting framework will clarify the role of cloud analysis in convective-scale ensemble prediction. To address these research gaps, this study evaluates a time-stepped hydrometeor initialization scheme based on cloud analysis using multi-source remote sensing data. Building upon traditional initial perturbations, this scheme independently runs high-resolution cloud analysis for each ensemble member, generating a three-dimensional hydrometeor increment field tailored to its own atmospheric state from the ingested radar and satellite retrievals. This increment is not introduced all at once at the initial time but is gradually added over the first few time steps of the model integration. This approach aims to achieve a smooth coordination between the hydrometeor field and the model's dynamic and thermodynamic framework. This study seeks to investigate: 1) How does this scheme influence the evolution of physical fields (e.g., heat, vertical motion) during the early stages of the model, and can it effectively shorten the "spin-up" time? 2) How does this approach affect the overall performance of the ensemble forecasting system, including the relationship between ensemble spread and root mean square error (RMSE), as well as the probabilistic forecasting skill for extreme precipitation thresholds (Zhang, 2018; Zhu et al., 2022).

The structure of this paper is as follows: Section 2 introduces the model, cloud analysis scheme, ensemble experiment design, and evaluation methods; Section 3 presents the comparison results and analyzes them from multiple perspectives, including overall skill and ensemble performance; Section 4 discusses the physical mechanisms, advantages, and limitations of the scheme in depth; Section 5 summarizes the main conclusions and outlines future research directions.

2. Methods and Experiment Design

This chapter details the numerical models, cloud analysis systems, core scheme implementation workflows, ensemble experiment design, evaluation methods, and data sources employed in this study.

2.1. Multi-Scale Singular Vector and Observation Perturbation Fusion Initial Condition Perturbation Scheme in Convective-Scale Ensemble Forecasts

This study employs the China Meteorological Administration(CMA)'s operational Global/Regional Data Assimilation Forecasting System-Mesoscale Model (CMA-Meso) for Convective-Scale Ensemble Forecasts. This model has been utilized in numerous studies for high-resolution precipitation forecasting and has demonstrated reliable performance (Xue J S, Chen D H. 2008; Shen X S, et al.,2022). V5.1 serves as the core integration model with a horizontal resolution of 3 km, 51 vertical levels, 15 ensemble forecast members, and a 48-hour forecast lead time. No cumulus parameterization scheme is required, allowing explicit circulation development. The forecast domain spans 107.7°–132.3°E longitude and 13.375°– 36.625°N latitude. The CMA global ensemble forecast system(CMA-GEPS) provides initial multiscale singular vector(SV) perturbations(Liu et al.,2024) and lateral boundary perturbations, with model perturbations implemented using the SPPT scheme. Physical processes configured as: WSM6 cloud microphysics, RRTM longwave radiation, Dudhia shortwave radiation, Monin-Obukhov near-surface layer, Noah land surface process, MRF boundary layer, shallow convective cumulus parameterization. The initial perturbation method for convective-scale ensemble forecasting employs a hybrid approach combining multiscale singular vector perturbation with observation perturbation analysis fields. This scheme comprises the following components:

2.1.1. Multi-Scale Singular Vector Perturbation

Considering the multi-scale characteristics of initial errors, a multiscale initial perturbation method based on singular vectors (SVs) is developed within the framework of CMA-GEPS to represent initial uncertainties. This approach involves computing multiscale SVs at varying resolutions using multiple linearized physical processes, aiming to capture rapidly growing perturbations ranging from mesoscale to synoptic scales in targeted regions. These SVs are then combined through a Gaussian sampling method with amplitude coefficients to construct the initial perturbations(Liu et al.,2024).The SVs initial perturbation method is outlined as follows:

Singular vectors are the set of disturbances that exhibit the fastest growth within a given time interval in a linear model, and the calculation can be mathematically formulated as maximizing the ratio of the evolved perturbation vector norm to the initial perturbation vector norm,as shownin Eq.(1):.

$$(L^{\mathrm{T}}\mathrm{P}^{T}EPL)x_i=\lambda_i^2 x_i \quad (1)$$

where E is the weight matrix that measures the perturbation magnitude, P is the projection operator, x_i is the i-th singular vector obtained from the solution, and λ_i is the corresponding i-th singular value. L^{T} is the transpose of the CMA global tangential linear model L, i.e., the adjoint model.

The CMA global singular vector employs the dry total energy definition for weighting matrix (Liu et al., 2013). The dry total energy model calculation formula for the CMA global mode singular vector is:

$$\boldsymbol{E}=\iiint_V \left(\frac{\rho_r\cos\varphi}{2}(u^{'})^2+\frac{\rho_r\cos\varphi}{2}(v^{'})^2+\frac{\rho_r\cos\varphi C_pT_r}{(\theta_r)^2}((\theta^{'})^{'})^2+\frac{\rho_r\cos\varphi C_pT_r}{(\Pi_r)^2}((\Pi^{'})^{'})^2\right)dV \quad (2)$$

Horizontal wind components (u，v), perturbation potential temperature (θ'), and perturbation dimensionless pressure (Π') correspond to perturbation quantities (expressed as: $u', v', (\theta')', (\Pi')'$ ）, $V=d\lambda d\varphi d\hat{z}$,where $\hat{z}$ is the terrain-following coordinate, λ and φ represent longitude and latitude in the model spherical coordinate system, respectively, and C_p is the specific heat of dry air at constant pressure. T_r 、 θ_r 、 Π_r and ρ_r denote the reference temperature, reference potential temperature, reference dimensionless pressure, and reference density, respectively.

Based on the the Tangent Linear Model (TLM) and Adjoint Model (ADM) within the CMA global 4DVar system, different scale SV initial perturbations with 1.5° horizontal resolution (optimized duration 24h) and 0.5° horizontal resolution (optimized duration 6h) are filtered and blended. These are dynamically downscaled into the convective-scale ensemble forecast model to generate initial fields formed by multi-scale SV initial perturbations. In constructing convective multi-scale singular vectors, based on the cross-scale of different variables at different levels, a 2-dimemsional discrete cosine transform (Denis et al., 2002) is employed to construct a multi-scale SV optimal spectral cutoff hybrid initial disturbance method(Zhang et al.,2015).

2.1.2. Observation Perturbation Method

Observation perturbations are randomly sampled based on observation errors for different observation types and meteorological elements, then superimposed on unperturbed observations to generate a set of slightly varying observations for ensemble assimilation analysis. As shown in Equation (3), R_n represents 14 random numbers sampled from a standard normal distribution, ε denotes the standard deviation of observation errors,, O_{ctl} denotes the unperturbed observation, and O_n denotes the 14 perturbed observations.

$$O_n=O_{ctl}+R_n\times\varepsilon \quad \text{n=1,2,...,14} \quad (3)$$

Observation errors for different observation types and meteorological elements exhibit distinct vertical structures. For instance, zonal wind observation errors generally increase with height in the troposphere, whereas temperature observation errors first decrease and then increase with height.

2.1.3. Multi-Scale Hybrid Perturbations

Analyzing the structure and error growth characteristics of initial value perturbations and observational perturbations across different scales, this study combines multi-scale optimal spectral truncation hybrid initial value perturbations with observational perturbations to construct an optimal fusion method for initial value perturbations. The specific formula is shown in (4), where j denotes the ensemble member, $SVperb_j$ represents the optimal spectral truncated hybrid initial perturbation from multi-scale SVs, $Obsperb_j$ is the observed perturbation, and$Perb_j$ is the optimal fused initial perturbation.

$$Perb_j=SVperb_j+Obsperb_j \quad (4)$$

2.2. Cloud Analysis Scheme

The cloud analysis system originated from the Data Analysis System (ADAS) of the Area Reporting and Prediction System (ARPS) (Brewster, 1996; Zhang,1999). Tailored to the characteristics of the CMA-MESO model, it incorporates optimized diagnostics and integrates multi-source domestic observations (Zhu et al., 2017). Based on cloud thermodynamic-dynamic principles and observational experimental relationships, it analyzes cloud initial field information and implements cloud-internal microphysical data assimilation through a relaxation approximation assimilation method.

Input remote sensing observations: The system ingests a diverse set of remote sensing data, including three-dimensional mosaic radar reflectivity, hourly averaged FY-2G satellite black-body temperature (TBB) products,FY-2G total cloud water (or total cloud cover) products, together with conventional ground-based observations. The fusion of these multi-source remote sensing data—radar and geostationary satellite—forms the foundation for the scheme’s effectiveness in initializing cloud and precipitation fields.

The cloud analysis scheme comprises several key functional components: three-dimensional cloud mass distribution analysis (grid-cell cloud cover), cloud type analysis, cloud particle (cloud water/ice) analysis, precipitation type discrimination, precipitation particle quantification, diagnostic balance, and thermal field coordination. The three-dimensional grid-cell cloud cover refers to the specific cloud mass magnitude at each model grid point. Based on background relative humidity information, a preliminary three-dimensional cloud cover distribution is established. The computational approach involves first calculating the lifting condensation level. Above this level, background cloud cover is estimated using the following exponential empirical relationship (Koch, S.E. et al., 1997):

$$\mathrm{VCF} = \left(\frac{RH-RH_0}{1.0--RH_0}\right)^b \quad (5)$$

where RH is the relative humidity provided by the background field, andRH_0 is a threshold value varying with altitude. Subsequently, the cloud base position is corrected based on ground observations to estimate cloud thickness; the cloud top position is corrected using satellite observations; cloud cover is adjusted based on radar echoes; and cloud types are classified according to temperature and static stability

The Smith-Feddes scheme(Smith,1990) is employed for analyzing cloud droplet particle content. The computational procedure involves dividing the cloud from base to top into multiple layers (e.g., every 100m). Temperature, pressure, and saturated vapor pressure are calculated layer by layer. The difference in saturated vapor mixing ratio between adjacent layers serves as the fundamental quantity for cloud water and cloud ice.It is assumed that these cloud water and ice particles rise to the next layer with vertical motion within the cloud. The basic cloud water and ice quantities for each layer can be expressed by the following formula, where k denotes the cloud layer, W_{VS} represents the saturated vapor mixing ratio, and $ALWC_k$ denotes the base mixing ratio quantity used to separate cloud water and ice within that layer.

$$ALWC_k = ALWC_{k-1} + W_{vs_{k-1}} - W_{vs_k} \quad (6)$$

The analysis of precipitation particles is primarily divided into two steps. The first step involves distinguishing precipitation types within the radar echo range based on wet-bulb temperature and ambient field temperature. The second step entails quantitative analysis of precipitation particles. Within different precipitation types, the relationship between echoes and various precipitation forms is utilized to determine the specific precipitation type (including rain, snow, and hail).

2.3. Initial Assimilation Scheme

Newtonian relaxation (nudging) technique is employed for assimilation program design. This involves introducing a “forcing term” during the assimilation period of model integration. This forcing term is proportional to the deviation between model forecast values and observed values, with the proportionality coefficient serving as the relaxation factor. Relaxation approximation adjusts the model’s background field to observations distributed within the time window(ten steps, the model integration interval is 30 second), yielding an analysis field that satisfies both model dynamical constraints and observational fit, thereby achieving intra-cloud information initialization.

$$\frac{\partial q}{\partial t} = \sum F_i + \alpha \times (q_{v-q}) \quad (7)$$

The assimilated variables include water vapor, cloud water, cloud ice, rainwater, snow, etc. q is the cloud microphysical forecast variable sent to the assimilation approximation; $\sum F_i$ represents all other physical effects in the model forecast equations; α is the relaxation approximation coefficient; q_v is the value obtained from the cloud microphysical analysis at the corresponding time. Using a linear decay scheme, it is gradually increased to the corresponding integral variable, with the assimilation window designed for 10 steps

2.4. Experimental Design

Studies have demonstrated the positive role of cloud analysis in improving short-term precipitation forecasts. (Zhao and Xue, 2009; Pan and Xue, 2020). To compare the impact of hydrometeors introduced via cloud analysis schemes on convective scale ensemble forecasting systems, two sets of control experiments were designed. The control group (CTL) employed standard ensemble forecasting without cloud analysis schemes. Initial perturbations with Multi-scale Singular Vector and Observation Perturbation Fusion Scheme were applied only to conventional dynamic, thermal, and moisture fields. For the experimental group(EXP), after applying previous initial perturbations to each ensemble member, the cloud analysis module was additionally run to generate an independent set of three-dimensional hydrometeor fields (cloud water, rainwater, ice water, etc.) for each member. For each ensemble member, during the first 10 time steps of model integration (i.e., the initial 5 minutes), the incrementally generated hydrometeors from the cloud analysis were progressively added to the model forecasted hydrometeor field using either a linear or specific weighting function(Nudging).The ensemble forecast comprises 1 control forecast and 14 perturbed forecasts, totaling 15 ensemble members. It runs twice daily at 00:00 UTC and 12:00 UTC for 48-hour forecasts, with model data output at 1-hour intervals. Validation data includes conventional soundings, surface stations, radar precipitation, and satellite cloud products.

The selected test period—August 3 to 7, 2025—features a heavy rainfall event affecting southern China, particularly Guangdong and Guangxi. This extreme persistent precipitation event was triggered by an unusually stable weather system configuration, with rainfall at multiple extreme stations breaking records for that period. For example, the Nanao South Station in Longgang District, Shenzhen recorded a maximum point rainfall of 769 mm. The affected area was extremely extensive, with precipitation spanning most of Guangdong and Guangxi, with cumulative rainfall exceeding 100 mm across an area of 193,000 square kilometers. All 21 cities in Guangdong Province experienced heavy rainfall, with 12 cities experiencing exceptionally heavy rainfall, resulting in extreme, persistent, and highly efficient precipitation. This torrential rain was the result of prolonged, stable interaction among multiple weather-scale systems. Primarily, the subtropical high pressure system was abnormally far north, large, and stable , blocking the eastward movement of weather systems and causing the rainfall system to linger. A strong easterly airflow persisted south of it. The southwest flow and easterly flow formed a low-pressure trough system that lingered for an extended period, providing sustained, large-scale dynamic lifting conditions. The southwest monsoon was unusually strong, with an active low-level jet stream transporting nearly uninterrupted moisture from the South China Sea and the Bay of Bengal. The coastal shoreline and the Nanling Mountains to the north acted as barriers, forcing the convergence and lifting of warm, moist air at lower levels, further intensifying precipitation efficiency(Figure 1).

doi:10.20944/preprints202605.1096.v1

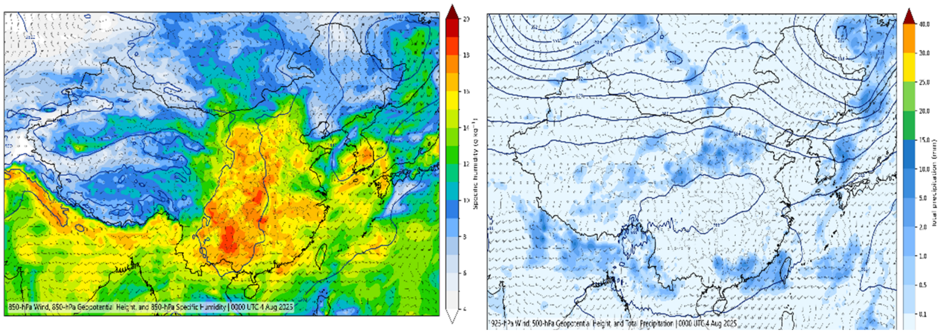

Figure 1. Physical parameter diagnostic map of heavy precipitation over South China (a) 850-hPa wind vectors (barbs, m s^{-1}), geopotential height (contours, gpm), and specific humidity (shaded, g kg^{-1}) at 0000 UTC 4 August 2025. (b) 500-hPa geopotential height (contours, gpm), 925-hPa wind vectors (barbs, m s^{-1}), and 24-h accumulated precipitation (shaded, mm) ending at 0000 UTC 4 August 2025.

2.5. Evaluation Methods

Statistical tests for continuous variables were evaluated using the model's own analysis fields as ground truth. Precipitation forecasts were validated using observational data from over 2,400 stations provided by the National Meteorological Information Center of the China Meteorological Administration.

2.5.1. Root Mean Square Error, Ensemble Dispersion, and Consistency Score

Root Mean Square Error (RMSE) is a scoring method reflecting the discrepancy between forecast and observed values. A smaller value indicates better forecasting performance.

$$RMSE = \sqrt{\frac{1}{n}\sum_{i=1}^{n}(y_i - o_i)^2 (1.1)} \quad (8)$$

where y_i is the forecast value for the i-th ensemble member, o_i is the corresponding observed or analysis value, and n is the total number of ensembles.

The ensemble spread represents the deviation of each ensemble member relative to the reference field, reflecting the uncertainty of the ensemble forecast compared to the reference field.

$$spread = \sqrt{\frac{1}{N}\sum_{i=1}^{N}(y_i - y)^2} \quad (9)$$

The meaning of variables in above formula is just same to that of RMSE except that the y indicate ensemble mean or control of the ensembles. In daily operations, the relationship between ensemble mean root mean square error (RMSE) and ensemble forecast dispersion (consistency score, Consistency = spread/RMSE is commonly used to assess the reliability of ensemble forecasting systems. Higher consistency between the ensemble mean RMSE and ensemble dispersion indicates greater system reliability.

2.5.2. Continuous Rank Probability Score Continuous Rank Probability Score (CRPS)

CRPS is commonly used to describe the overall error between forecast and observed cumulative distributions, measuring differences in ensemble forecast performance across various lead times. A lower CRPS score indicates better performance of the forecast system.

$$CRPS(P, X_a) = \int_{-\infty}^{\infty}[P(x) - P_a(x)]^2\,\mathrm{d}x \quad (10)$$

where X_a is the observed value, x is the forecast value, and P and P_a are the cumulative distributions of the ensemble probability forecast and the observed true value, respectively.

doi:10.20944/preprints202605.1096.v1

2.5.3. Brier Score

The Brier Score (BS), also known as the Mean Probability Error, is a method for evaluating the deviation between ensemble probability and true observation probability. Its value ranges from 0 to 1 and is a negativesigned score.

$$BS = \frac{1}{N}\sum_{n=1}^{N}(p_n - o_n)^2 \quad (11)$$

where N is the total number of events occurring, $\mathrm{p_n}$ is the predicted probability of the event being detected in the nth sample, and $\mathrm{o_n}$ is the observed frequency. Furthermore, the BS score is highly dependent on sample frequency

2.5.4. Area Under the ROC Curve (AROC)

The Area Under the Relative Operating Characteristic (ROC) curve represents an application of Signal Detection Theory applied to ensemble forecasting. It serves as a test method for binary classification elements. At a specific grid point or station, it determines whether an event occurred based on actual conditions to evaluate forecasts, yielding accurate forecasts, false positives, and false negatives. AROC serves as a skill metric for ROC curves, reflecting a ensemble forecasting system's ability to distinguish specific threshold events (whether a model-forecasted event occurs or not). The ROC area ranges from 0 to 1, with higher scores indicating better precipitation resolution capability. An AROC greater than or equal to 0.5 indicates positive skill in probabilistic forecasting. Perfect forecasts yield an AROC of 1, while forecasts with no skill yield an AROC of 0.5.

3. Results Analysis

The core objective of this study is to develop a time-step hydrometeor initialization scheme suitable for ensemble forecasting, driven by multi-source remote sensing data. For each ensemble member, the cloud analysis system runs independently based on its distinct initial fields (wind, temperature, humidity, pressure) and ingests three-dimensional mosaic radar reflectivity, hourly averaged FY-2G satellite black-body temperature (TBB), and FY-2G total cloud water products to generate member-specific hydrometeor fields. Because the cloud analysis system loads the corresponding ensemble member's initial field information, the resulting hydrometeor fields (qr, qc, qi, qs, qg) are physically consistent with each member's own atmospheric state, thereby introducing reasonable uncertainty in the hydrometeor initial fields directly constrained by radar and geostationary satellite observations.

A Newtonian relaxation (nudging) technique is used to distribute the total hydrometeor increment across the first N time steps of the model integration (in this test, N=10, integration time step 30 seconds), corresponding to gradually incorporating the hydrometeor mass into the model variables over the first 5 minutes after model startup using a smooth weighting function. This approach minimizes dynamic imbalances caused by the "injection" of a large amount of hydrometeors. During the hydrometeor injection, latent heat release is adjusted in real-time based on cloud phase states diagnosed from the ingested radar and satellite data(e.g., radar reflectivity profiles and FY-2G TBB-derived cloud top temperature), as well as the injected hydrometeor mass, to maintain thermal equilibrium.

Ensemble forecast validation aims to systematically assess the quality and performance of probabilistic forecast products, with its core focus on verifying whether the representation of forecast uncertainty is accurate and reliable.The validation leverages the same remote sensing observations (radar reflectivity, FY-2G TBB and cloud water products) as reference benchmarks, in addition to conventional surface and upper-air measurements. The evaluation not only examines overall accuracy (e.g., using Continuous Ranked Probability Score CRPS or Brier Score) but also emphasizes diagnosing the reliability (consistency between forecast probabilities and actual occurrence frequencies) and resolution (ability to distinguish different weather events) of probabilistic forecasts. By analyzing relative operating characteristic curves and ensemble dispersion-error relationships, one can diagnose systematic biases, insufficient dispersion, or overconfidence issues, thereby comprehensively evaluating the performance of the ensemble forecasting system. This study examines the impact of remote sensing-derived hydrometeor initialization on regional ensemble forecasting from both ensemble averaging and probabilistic forecasting perspectives.

3.1. Impact on Surface Element Forecast Results

As shown in Figure 2, the open sea area within the 10-meter wind analysis field is dominated by southwesterly winds. Due to topographical influence, the terrain of Taiwan induces strong convergence on the airflow, resulting in pronounced low-level shear that readily triggers localized storms. Both experiments could reasonably simulate the overall direction and magnitude of the analysis field's wind speed. However, the forecast results showed a slightly easterly bias in wind direction compared to the analysis field, despite the overall southwest wind pattern. Two cyclonic circulations were present southeast of the test area (approximately 15N, 130E) and at its northernmost edge (35N, 127E), corresponding to the analysis field. Comparatively, the cloud analysis test exhibited slightly higher wind field dispersion in the heavy precipitation zones of South China (including Guangxi, central and eastern coastal Guangdong, etc.).The trough shear in South China remains stable, with a pronounced low-level jet stream, leading to heavy to extremely heavy rainfall.

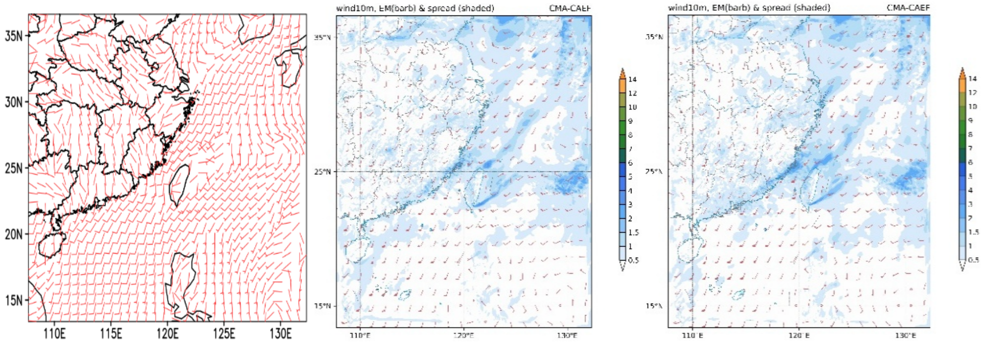

Figure 2. Surface 10-m wind valid at 00:00 UTC on August 4, 2025: analysis field (a); 24-hour forecasts initialized 24 hours earlier (00:00 UTC on August 3, 2025): without cloud analysis (b) and with cloud analysis (c).

Regarding process precipitation forecasting capability, the 24-hour cumulative precipitation from 00:00 on August 3, 2025, shows a core area of heavy precipitation along the South China coast (Fujian/Guangdong border) and eastern Taiwan, with some areas exceeding 100 mm. For this case, both ensemble forecasting experiments demonstrated predictive capability for this precipitation event. However, the control experiment's precipitation coverage was narrow, extending only to central-southern Guangdong and failing to capture the intense precipitation band along the Fujian coast. Intensity was significantly underestimated, with the ensemble mean forecast at just 50mm (dark blue zone), markedly lower than the observed 100mm+. Probabilistic forecast results (figure omitted) showed no ensemble member predicting precipitation exceeding 100mm.Forecast uncertainty was high, with densely clustered dispersion contours indicating unstable model predictions for precipitation location and intensity. Cloud analysis forecasts showed precise coverage of the precipitation band: accurately predicting the intense precipitation center along the Fujian coast (near 115°E), while the intense precipitation area along the Guangdong coast (near 118°E) also showed thicker overlap, with more reasonable intensity and location, though the intense precipitation center near Guangzhou was weaker.

doi:10.20944/preprints202605.1096.v1

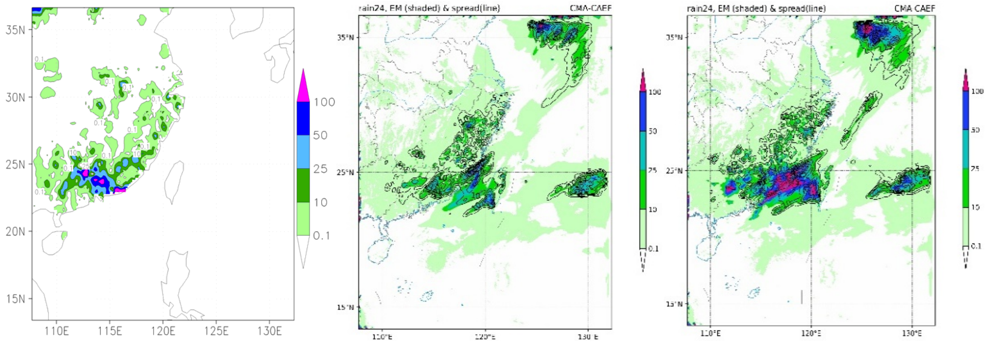

Figure 3. Observations (left) and ensemble mean/spread of 24-hour precipitation forecasts initialized at 00:00 UTC on August 3 without (middle) and with (right) cloud analysis.

Figure 4 shows the core area of the 24-hour cumulative precipitation forecast for August 5, 2025, centered on the coastal regions of Fujian and Guangdong, with precipitation exceeding 100 mm. The cloud-free experiment (middle panel) exhibits poor agreement with the actual conditions: the actual heavy precipitation band along the Fujian coast was significantly underestimated in the forecast. Probability <40%, resulting in missing high-risk areas, indicates the model’s insufficient sensitivity to heavy precipitation triggering mechanisms; coastal Guangdong precipitation bands were forecasted reasonably well, but their coverage was narrower.(Did not extend to the Fujian coast). The cloudy test showed high agreement with actual conditions: in areas with actual precipitation >100mm (e.g., Fujian coast, Guangdong coast), the precipitation probability in the cloudy test was generally >80%, indicating the model’s ability to accurately identify heavy precipitation risk zones.For Fujian coastal areas (116°E, 28° N) with >100mm precipitation, the cloud-based test forecast probability exceeded 90%; for Guangdong coastal areas (119°E, 22°N), the forecast probability exceeded 80%. Only some heavy precipitation areas in Guangdong were slightly overestimated. Analysis of ensemble precipitation forecasts from different initialization times reveals that the cloud analysis scheme provides coordinated hydrometeor variables at model start, enabling near-instant precipitation onset and significantly reducing model spin-up time. In contrast, the non-cloud analysis process requires extended initialization, resulting in markedly delayed precipitation onset.

Overall, precipitation forecasts indicate that the location and track of the main rain band in the cloud analysis experiment closely match actual conditions, with no widespread false precipitation; the intensity and distribution of the center of extreme precipitation are depicted more accurately, successfully capturing the characteristics of localized heavy precipitation observed in reality; the distribution of ensemble dispersion is more reasonable, with uncertainty concentrated in key precipitation areas, which better aligns with the physical logic of convective-scale ensemble forecasting.

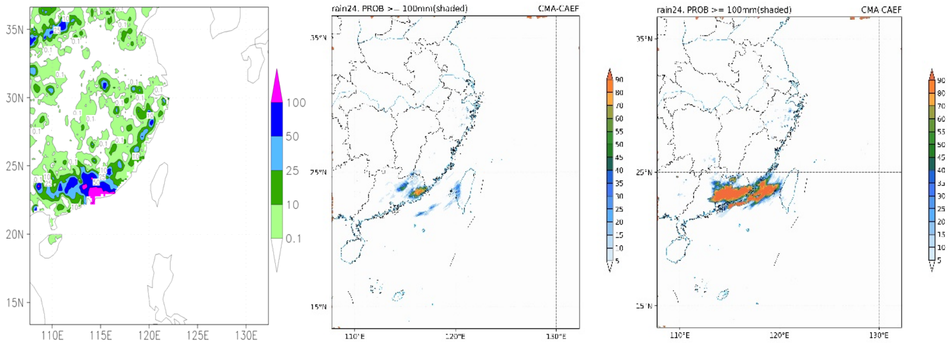

Figure 4. Observations (left) and the probability of 24-hour accumulated precipitation exceeding 100 mm from forecasts initialized at 00:00 UTC on August 4 without (middle) and with (right) cloud analysis.

3.2. Improvements to Ensemble Averaged Forecast Results

To compare differences between two convective-scale ensemble forecast experiments, the spatiotemporal evolution of RMSE and BIAS for different variables and ensemble levels were analyzed. RMSE, the square root of the mean square error between forecast and observed values, reflects both random and systematic errors in forecasts, serving as a measure of total error. Comparison of RMSE and BIAS for the 500 hPa geopotential height field during the experiment period, with and without cloud analysis: The RMSE of the 500 hPa potential height fields for both experiments exhibited a monotonically increasing trend with forecast lead time, but there were significant differences in the rate and magnitude of error growth: for the CTL experiment (blue dashed line), the RMSE was 3.4 m at a 12-hour lead time and increased rapidly with lead time, reaching 6.8 m at the 48-hour lead time, with a cumulative error rate of approximately 0.09 m/h. In the Cloud experiment (red solid line), the RMSE at the 12-hour lead time was slightly higher than that of the CTL experiment (approximately 3.8 m), but the rate of error increase slowed significantly. After the 24-hour lead time, the RMSE remained lower than that of the CTL experiment, and at the 48-hour lead time, the RMSE was only 6.3 m, with the cumulative error rate decreasing to 0.05 m/h. This indicates that the cloud analysis scheme effectively suppresses the nonlinear growth of forecast errors over medium- to long-range time scales .Evolution of forecast bias (Bias) (lower half of Figure 5): The ensemble forecast bias of the two sets of experiments exhibits completely different systematic characteristics: CTL experiment (left panel): The bias of the ensemble mean and ensemble members remains near 0 within the 12–24 h forecast lead time, then rapidly shifts toward a positive bias after 24 h; stabilizing in the 1–2 m range between 36 and 48 hours, exhibiting a distinct systematic overestimation, with a relatively high dispersion in the bias distribution among ensemble members. Cloud experiment (right figure): The ensemble mean bias exhibits a slight negative deviation within the 12–24-hour timeframe (with a bias of approximately -2 m at 24 hours), followed by a rapid rebound; after 36 hours, it stabilizes near 0, with the systematic bias significantly weakened. Meanwhile, the distribution of member biases is more concentrated, with a dispersion notably smaller than that of the CTL experiment, resulting in significantly improved forecast consistency and stability.

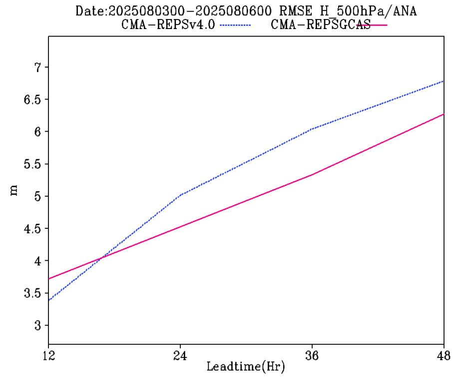

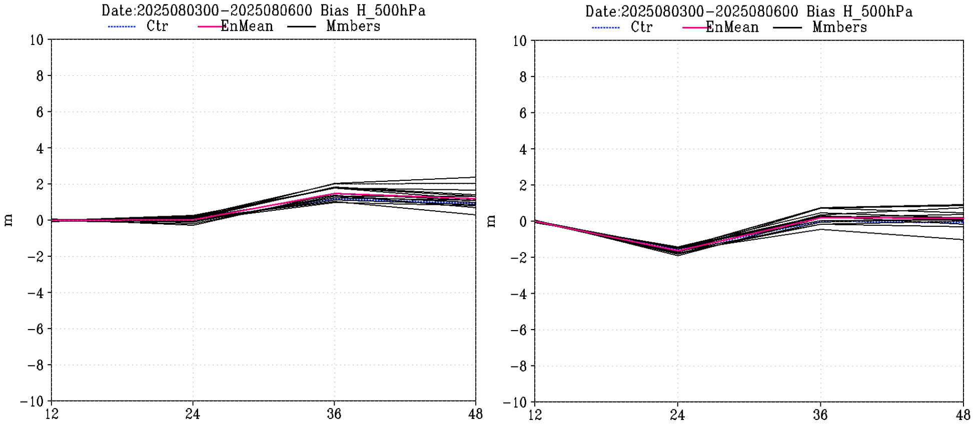

Figure 5. Comparison of the root mean square error (RMSE, top) and BIAS (bottom) of the 500 hPa geopotential height field between experiments without (bottom left) and with (bottom right) cloud analysis during the experimental period.

The evolution of the 850 hPa temperature field forecast RMSE with lead time for both experiments is shown in the Figure 6. Overall, the RMSE for both experiments exhibited a monotonically increasing trend as the forecast lead time extended, consistent with the fundamental principle that numerical forecast errors accumulate with integration time. The RMSE of the control experiment increased from approximately 0.66 K at a 12-hour lead time to approximately 0.96 K at a 48-hour lead time; the RMSE of the cloud analysis experiment increased from approximately 0.72 K at a 12-hour lead time to approximately 0.94 K at a 48-hour lead time. Comparisons between the experiments reveal significant stage-specific differences in error performance: within the short-term forecast horizon of 12–30 h, the RMSE of the cloud analysis experiment is slightly higher than that of the control experiment, with the difference peaking at the 12-hour forecast horizon (approximately 0.06 K) and gradually narrowing as the forecast horizon extends; In the medium-to-long forecast horizon of 30–48 h, the RMSE of the cloud analysis experiment surpassed that of the control experiment, demonstrating superior forecasting performance; at the 48-hour forecast lead time, the RMSE was approximately 0.02 K lower than that of the control experiment. Further analysis of the error growth rate reveals that the error growth slope of the control experiment remained generally stable, whereas the error growth rate of the cloud analysis experiment slowed significantly after 30 hours.

The evolution of the 850 hPa temperature field forecast bias with lead time for both experiments is shown in the Figure 6 too. Both the ensemble mean of the control and cloud analysis experiments, as well as the control forecast, exhibit consistent systematic cold bias characteristics: the bias is 0 K at the 12-hour lead time, then rapidly decreases, reaching a peak cold bias at the 24-hour lead time, after which the bias slightly rebounds and stabilizes, maintaining a cold bias level of approximately -0.3 to -0.4 K at the 48-hour lead time. A comparison of the two sets of experiments reveals that the peak cold bias in the cloud analysis experiments is slightly greater than that in the control experiments; however, there are no significant differences in the overall evolution patterns, magnitude, or inter-member variability of the biases between the two groups. This indicates that cloud analysis has a limited impact on the systematic bias characteristics of the 850 hPa temperature field.

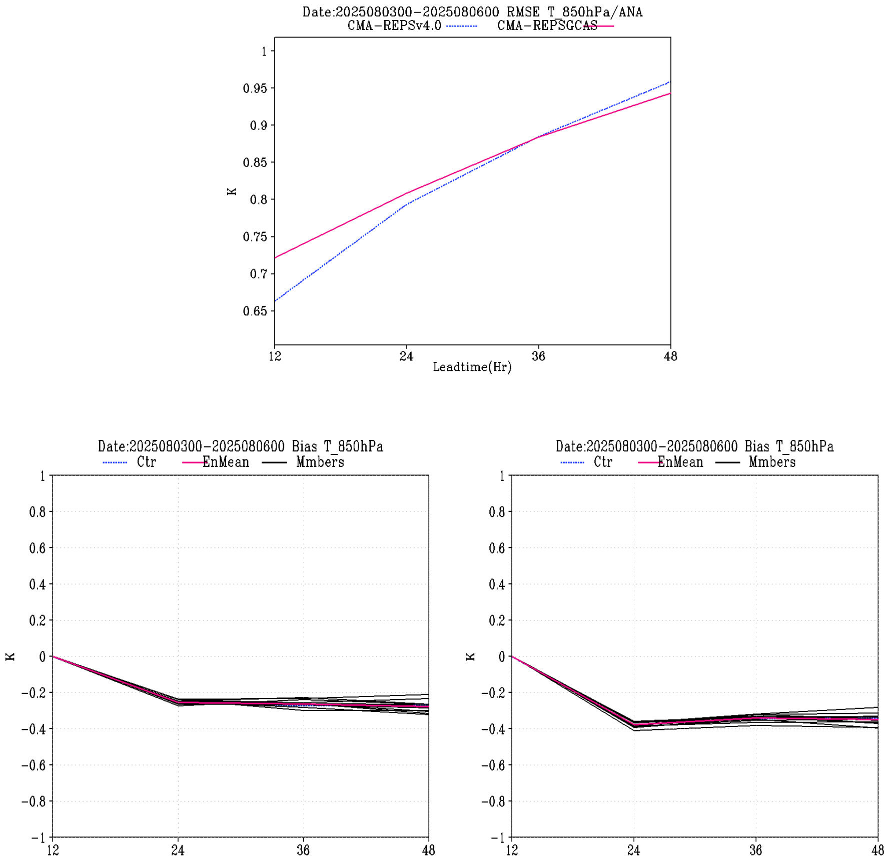

Figure 6. Comparison of the root mean square error (RMSE, top) and BIAS (bottom) of the 850 hPa temperature field between experiments without (bottom left) and with (bottom right) cloud analysis, as a function of forecast lead time during the experimental period. (units: K).

The RMSE of the 250 hPa meridional wind (Figure 7) shows that the overall trend of RMSE for both experiments continues to increase with the forecast lead time (12–48 hours), consistent with the pattern of numerical forecast errors increasing over time. The RMSE of the control experiment increased from approximately 2.9 m/s at the 12-hour lead time to approximately 4.2 m/s at the 48-hour lead time; the RMSE of the cloud analysis experiment increased from approximately 2.7 m/s at the 12-hour lead time to approximately 4.15 m/s at the 48-hour lead time. Throughout the entire forecast period, the RMSE of the cloud analysis experiment was consistently lower than that of the control experiment, with more significant improvements observed in the short-term forecast period (12–30 h): the RMSE decreased by approximately 0.2 m/s at the 12-hour forecast lead time and maintained an advantage of approximately 0.05 m/s at the 48-hour forecast lead time, indicating that cloud analysis provides a stable improvement in the accuracy of upper-level wind field forecasts. Regarding the trend of error growth, both sets of experiments showed a rapid increase in error within the 12–36-hour forecast horizon, with the growth rate slowing down in the 36–48-hour period. The error growth slope of the cloud analysis experiment was slightly lower overall than that of the control experiment, demonstrating superior error control capability.

Regarding the 250 hPa wind component BIAS, the cloud-free analysis test showed a BIAS close to 0 at the initial time (12 hours). Over time, the BIAS dispersion of ensemble members (black line) increased significantly, with both positive and negative deviations appearing. At 48 hours, the BIAS of some members reached ±0.8 m/s.The ensemble mean (red line) and control forecast (blue line) maintained BIAS values close to zero with minimal fluctuations, indicating the ensemble mean effectively counteracts positive and negative deviations among members. At the initial moment of the cloud-analysis experiment, BIAS was similarly close to 0. BIAS dispersion among ensemble members also increased over time, but a distinct fluctuation peak appeared around 36 hours, followed by a slight decline. This suggests cloud analysis may have increased uncertainty among ensemble members, but this uncertainty was offset in the ensemble mean. Both the ensemble mean and control forecast maintained BIAS near zero, with fluctuations similar to those without cloud analysis. This indicates the ensemble mean's effective bias cancellation in both experiments. At 250 hPa—the upper troposphere—cloud presence directly impacts radiative and dynamic processes. Cloud analysis likely provides a more accurate characterization of these processes, thereby improving upper-level wind field forecasts.

Cloud analysis directly corrects cloud fields in the lower and middle stratosphere; the improvement in the wind field at 250 hPa is an indirect effect, but it still demonstrates a consistent advantage, consistent with the physical law that numerical forecast errors propagate with height and over integration time.

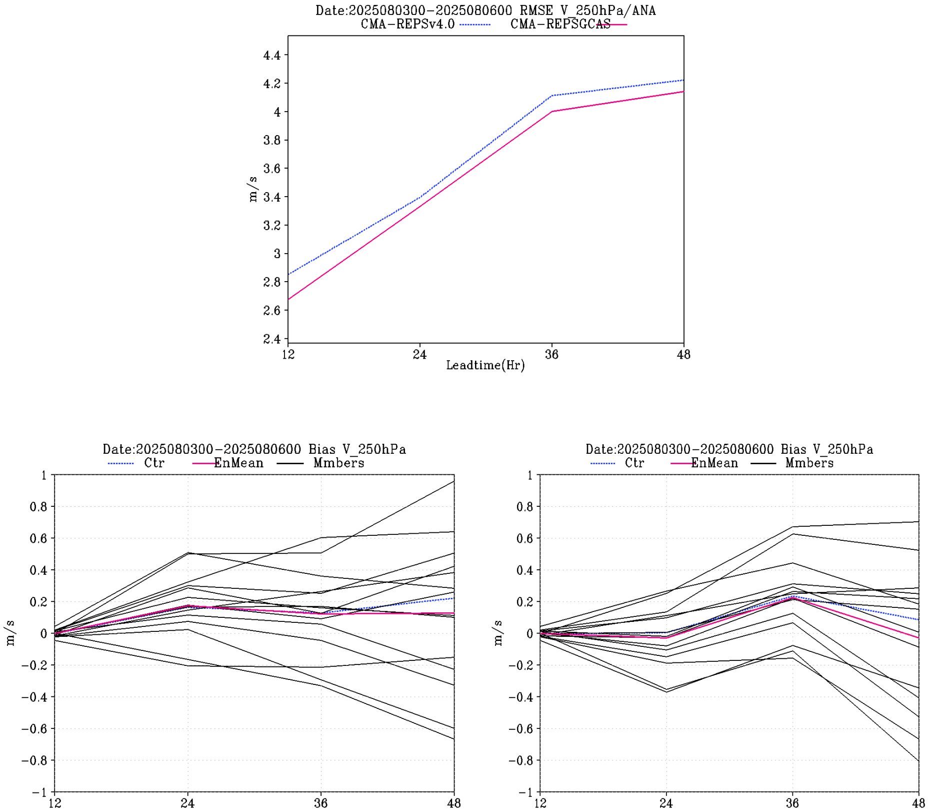

Figure 7. Comparison of the root mean square error (RMSE, top) and forecast bias (BIAS, bottom) of the 250 hPa meridional wind component (V) between experiments without (bottom left) and with (bottom right) cloud analysis, as a function of forecast lead time during the experimental period. (Unit: ms $^{-1}$).

3.3. *Enhancing Probabilistic Forecasting Skills*

Evaluating probabilistic forecast skill is a multidimensional process aimed at assessing whether the probability distribution of forecasts is accurate and useful. It primarily encompasses reliability, resolution, and overall accuracy, which are interrelated and collectively form a complete description of skill.

3.3.1. Impact on Surface Element Forecasts

Surface forecasts are a key focus of regional modeling. Based on the CRPS scores for the 10m u-component wind at the surface (Figure 8), the forecast values for both experiments monotonically increased with lead time (12–48 hours), indicating that the accuracy of probabilistic forecasts declines as the forecast lead time increases. The CRPS values for the cloud analysis experiments consistently remained lower than those for the no-cloud analysis experiments. For instance, at 48 hours, the pink line was approximately 1.17 m/s, while the blue line was about 1.23 m/s. This indicates higher accuracy in probabilistic forecasting of the 10m U component at the surface for the cloud analysis experiments. The spread for both experiments increased with time, consistent with the pattern of increased spread in ensemble forecasts as forecast lead time extends. The spread of the cloud analysis experiment in the cloud analysis tests was higher before 36 hours, but no higher cloud analysis was observed at 48 hours. The dispersion trend broadly matched the CRPS growth pattern, suggesting that the uncertainty estimation of the ensemble forecast aligned well with the increase in forecast errors.

For the 2m temperature, the CRPS values for both experiments rose between 12 and 36 hours, then began to decline after 36 hours. This indicates that forecast accuracy reached its lowest point in the mid-term and improved slightly in the late-term during this exprimnt. The CRPS values for the cloud analysis experiment consistently remained lower than those for the clear-sky analysis experiment. For example, at 36 hours, the cloud analysis yielded approximately 0.78 K while the clear-sky analysis yielded approximately 0.82 K, indicating superior probabilistic forecast accuracy for 2m temperature in the cloud analysis experiment. Spread for both experiments continued to increase over time without showing a decline in CRPS. The dispersion of the cloud analysis experiment was slightly lower than that of the no-cloud analysis experiment in the later period (24–48 hours), indicating that for cloud analysis tests, there introduces a reduction in initial uncertainty due to the constraining effect of observations. This outcome demonstrates that increasing spread is not the ultimate goal, cloud analysis raises the overall “skill ceiling” of the ensemble system, allowing it to perform better even with a slightly reduced spread.

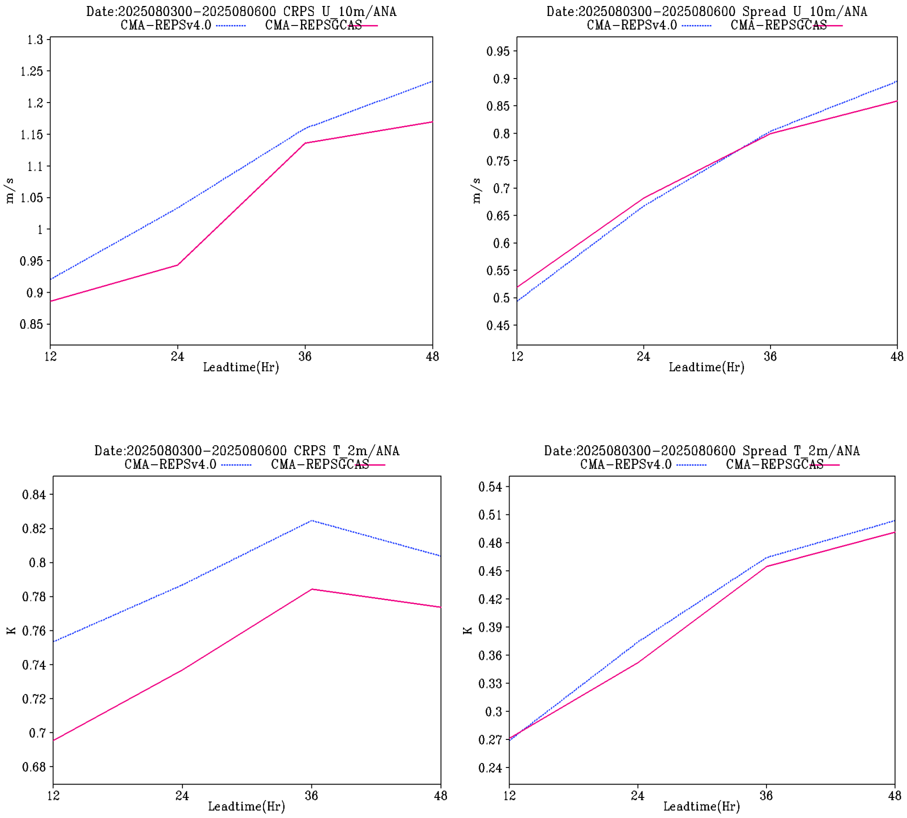

Figure 8. Comparison of the 10-meter wind U-component (top) and 2-meter surface temperature (bottom) for CRPS (left), SPREAD (right) evolution with forecast lead time.

AROC serves as a skill metric for ROC curves, reflecting the ensemble forecasting system's ability to distinguish specific threshold events (whether a forecast event occurs or not). The overall trend shows that the AROC scores for precipitation events of three intensity levels (light rain, moderate rain, heavy rain) decrease continuously with increasing forecast lead time (12–48 hours), indicating that longer lead times yield weaker discrimination capabilities regarding precipitation occurrence(Figure 9). Regarding the scale of the scores, smaller precipitation events exhibit higher initial AROC scores and slower subsequent decline rates; larger events show lower initial scores and faster decline rates. For example, at 48 hours, light rain's AROC is approximately 0.68–0.69, moderate rain is about 0.63–0.64, and heavy rain is roughly 0.61–0.62. The order consistently remains: light rain > moderate rain > heavy rain. The experimental difference is the cloud analysis test's AROC score, which is significantly higher than the non-cloud analysis test across all intensity levels and time periods. This advantage is more pronounced in heavy precipitation (moderate to heavy rain) forecasts. This indicates that cloud analysis effectively enhances the resolution of precipitation probability forecasts, with particularly significant improvements for heavy precipitation.

The Brier score is a commonly used metric in ensemble forecasting, representing the mean squared probability error—the deviation between ensemble probabilities and actual observed probabilities with lower values indicating better accuracy. A smaller value is better; 0 indicates perfect forecasting, while 1 indicates complete failure. The overall trend of precipitation mean squared probability error (BS) (right column, three figures: light rain, moderate rain, heavy rain) shows that the BS scores for all three precipitation intensity level s first increase and then decrease over time, peaking around 36 hours(Figure 9). This indicates that the mean squared probability error is larger in the mid-term and undergoes slight adjustments in the later period. The larger the precipitation intensity, the greater the fluctuation in BS scores, reflecting that the probability forecast error for heavy precipitation is more unstable. The BS scores for both experiments remained very close during most periods, with a relatively noticeable difference only at the 12-hour forecast. However, in practice, the BS scores for both ensemble forecasting experiments were very close to zero across different precipitation periods and forecast lead times, indicating that forecast errors were small for all precipitation intensity levels.

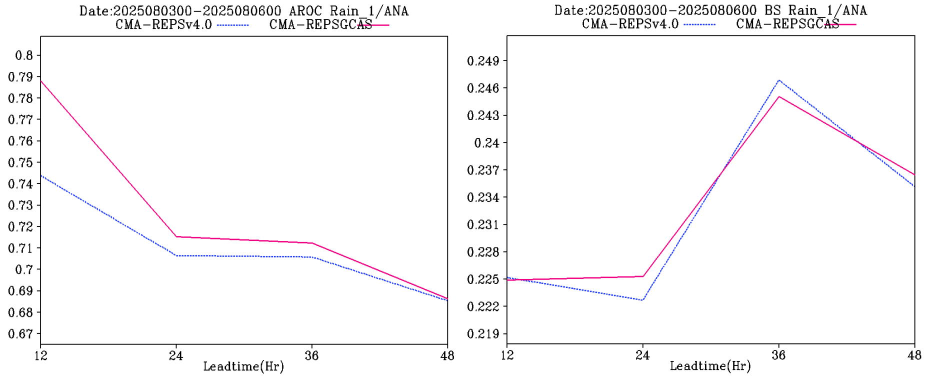

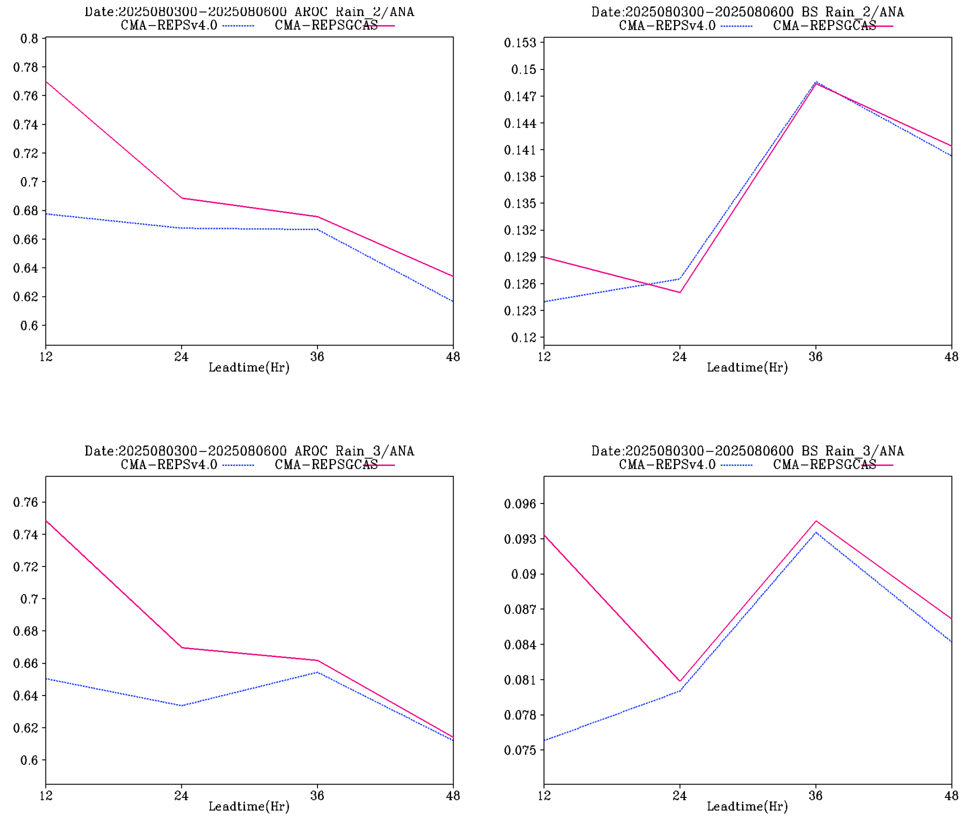

Figure 9. Comparison of AROC (left) and BS (right) scores for 6-hour accumulated precipitation from ensemble forecasts under cloud-free analysis conditions: (top) light rain (0.1 mm/6 h), (middle) moderate rain (4 mm/6 h), (bottom) heavy rain (13 mm/6 h).

3.4. Comprehensive Scorecard

The comprehensive scorecard evaluates a model's overall forecasting performance by conducting a combined assessment of isobaric surface elements and near-surface elements across two model systems. Its statistical test metrics employ significance testing methods to determine differences between models, while the scorecard itself reveals the comprehensive forecasting performance disparities among models. Specifically, the OUTLIER test quantifies the probability that the true analysis field (or observed value) at a given time falls outside the forecast range of all ensemble members. This probability corresponds to the first and last histogram values in the Talagrand diagram, reflecting the frequency at which the ensemble system completely fails to capture the actual weather condition (excluding it from the member distribution).This scorecard compares the forecasting performance of the clear-sky analysis (CMA-REPSv4.0) and the cloud-inclusive analysis (CMA-REPSGCAS) across different meteorological elements, height levels, and forecast lead times using distinct colors and symbols. Geopotential height shows only small patches of red during the initial 500 hPa period (12h), indicating that the cloud-free analysis is slightly superior. The remaining periods and height levels appear green or gray, suggesting that the cloud-inclusive analysis generally performs better in forecasting upper-level and mid-level potential heights.At upper-level (250 hPa) and mid-level (500 hPa) positns, Temperature shows predominantly green at 250hPa and 500hPa across most periods. At 850hPa, significant red appears only at 12h (solid triangle, 99.7% confidence level), indicating cloud-free analysis is superior only at the initial temperature time step for low-level forecasts, while cloud-inclusive analysis holds overall advantage for mid- and upper-level temperature forecasts. The U component is predominantly gray at 250 hPa and shows significant green (solid triangle) at 850 hPa. The V component exhibits significant green at 850 hPa, indicating that the cloud-inclusive analysis holds a clear advantage in forecasting low level wind fields, while differences in upper-level wind fields are not significant.

The near-surface element scorecard shows a pattern similar to the upper levels. The 2m temperature exhibits significant green (solid triangle) at 12h, with green or gray at other times, indicating that cloud analysis generally improves the forecast of 2m temperature. The 10m wind component (U10m) shows significant green (solid triangle) at 12h, while V10m is green for most periods, indicating that cloud-inclusive analysis yields better forecasts for near-surface wind fields. Regarding precipitation results for different intensity levels (0.1mm [light rain], 5.0mm [moderate rain], 15.0mm (heavy rain)), all three precipitation levels show significant green (solid triangles) during first 12 h,only 15.0mm precipitation exhibits small patches of red at 12h in concistency, indicating that cloud-based analysis outperforms in forecasting all precipitation levels, with pronounced improvement observed for heavy precipitation.

Overall, incorporating hydrometeor information derived from multi-source remote sensing data—including three-dimensional mosaic radar reflectivity,hourly averaged FY-2G satellite black-body temperature (TBB), and FY-2G total cloud water products—into the numerical model enables the dynamic framework to receive initial perturbations with more realistic latent heat distributions, leading to more accurate triggering, organization, and evolution of convective systems. At the same time, through continuous cyclonic assimilation of these radar and geostationary satellite observations, the cloud analysis scheme accumulates effects in adjusting temperature and humidity fields, bringing the model's large-scale environmental fields (such as humidity and instability) closer to actual conditions, thereby benefiting longer-term forecasts.

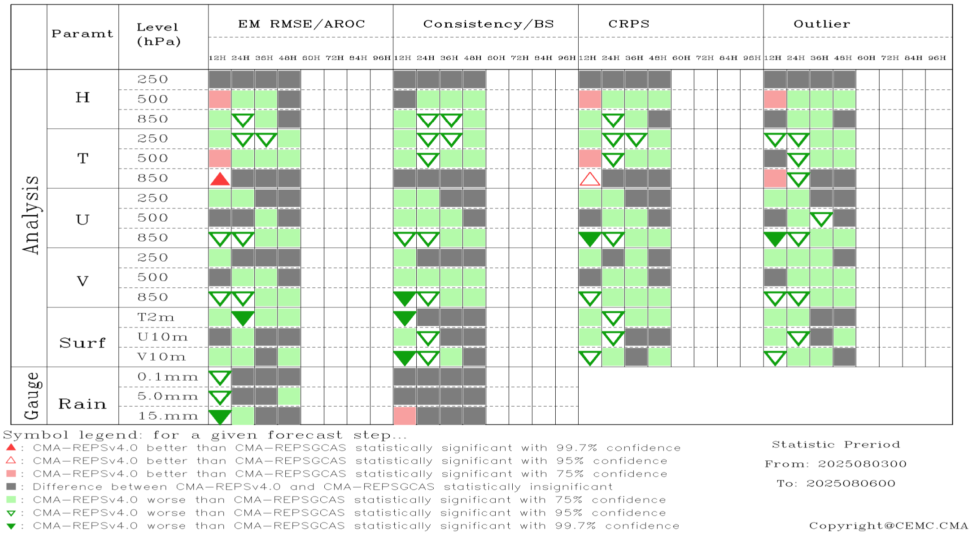

Figure 10. Integrated Scorecard.

4. *Mechanism Diagnosis of Cloud Analysis Impact on Convective-Scale Ensemble Forecasting Systems*

To analyze the mechanism by which cloud analysis influences convective-scale ensemble forecasting systems, this study conducts diagnostics separately for the impact of cloud analysis on individual members and on the ensemble forecast as a whole.

4.1. Mechanism Analysis of Cloud Analysis Impact on Individual Ensemble Member

This study includes two sets of comparative experiments with identical conditions except for the inclusion of cloud analysis systems. Based on the reflectivity-water vapor (Z-q) relationship, the cloud analysis process reconstructs the mixture ratio of cloud water, rainwater, and ice particles at grid points where echoes are observed, thereby directly generating cloud and precipitation material.

Subsequently, the model system performs critical thermodynamic adjustment steps through the nudging process: to ensure the thermodynamic validity of these implanted hydrometeors and to excite the corresponding dynamic fields, the system makes coordinated modifications to temperature and humidity within the cloud region based on the moist adiabatic process. Taking ensemble member 1, which began integration at 00:00 on August 3, as an example, this paper compares the differences with and without cloud analysis and the underlying physical reasons.

The cloud analysis process utilizes real-time observations (including satellite, radar, and ground reports) to introduce authentic, coordinated three-dimensional cloud (hydrometeor) and precipitation fields into the model initialization. Through this process, the mixture ratios of various hydrometeors (cloud water, rain, snow, etc.) are calculated, replacing or overwriting the corresponding grid values in the CMA-MESO model background field (Pan et al.,2016), thereby modifying the model initial conditions. However, simply implanting hydrometeor mass leads to physical inconsistencies. For instance, a sudden influx of cloud water into an unsaturated environment causes it to evaporate immediately, rendering the implant ineffective (the so-called "useless hydrometeor inversion").More critically, the latent heat release accompanying hydrometeor condensation/dewepoint processes remains unaccounted for, violating energy conservation and preventing the generation of a dynamic field matching observed convection (Duda et al., 2019). This necessitates triggering thermodynamic adjustments. A latent heat scheme must be employed to prevent immediate hydrometeor evaporation. The purpose of this scheme is precisely to enhance the presence of deep convection. The most fundamental method to prevent evaporation is to saturate the environment (Wallace and Hobbs, 2006). To achieve this objective, the cloud analysis performs a coordination adjustment step to make implanted hydrometeors (especially cloud water/ice) physically plausible, they must be assumed to form from condensation within an ascending air parcel. The system calculates the latent heat to be released and the water vapor to be consumed, achieving coordination adjustment by modifying the water vapor and temperature fields (Benjamin et al., 2016).Examining the temporal evolution of spatially averaged vertical distributions of precipitation from primary hydrometeors (cloud water: Figure 11 top; cloud rain: Figure 11 bottom), the cloud-free analysis experiment shows generally low cloud water content, with only minor variations between 500–700 hPa , peaking at approximately 2×10^{-5}. This distribution is confined to the middle troposphere, showing little temporal variation, while the lower troposphere (800–1000 hPa) exhibits virtually no cloud water signal. Cloud water content in the upper layer (100–300 hPa) was zero, indicating that the cloudless analysis failed to capture the presence of cloud water in the upper layer. In contrast, the analysis revealed that the cloud water content was significantly higher, with a more complete vertical distribution spanning from the lower to middle levels (400–900 hPa), forming a widespread distribution. The maximum value reached approximately 3×10^{-5}, exhibiting pronounced dynamic changes over time. Cloud water signals also appear in the upper levels (100–300 hPa) (approximately 1×10^{-5}), indicating that cloud analysis can more accurately reflect the vertical structure of clouds. The cloud-free analysis shows extremely low rainfall content, with only scattered distributions present between 500–800 hPa and a maximum value of approximately 1×10^{-5}. The lower levels (800–1000 hPa) exhibit virtually no rainfall signal, failing to form a distinct vertical structure. This indicates that the cloud-free analysis struggles to simulate the precipitation formation process. This occurs because numerical models without cloud analysis inherit coarse-resolution initial fields from global models, which cannot effectively assimilate mesoscale information like clouds and precipitation. Consequently, mesoscale models integrate from a state devoid of water condensation, relying solely on their own physical processes (cumulus parameterization, microphysics) to gradually form clouds and precipitation and inherently delays the precipitation formation process. In contrast, cloud analysis directly incorporates real cloud and precipitation data, drastically shortening or even eliminating the spin-up phase. This enables the model to possess realistic precipitation capabilities from the outset, allowing for more accurate simulation of cloud and precipitation formation processes, which is crucial for short-term nowcasting and severe convective weather warnings.

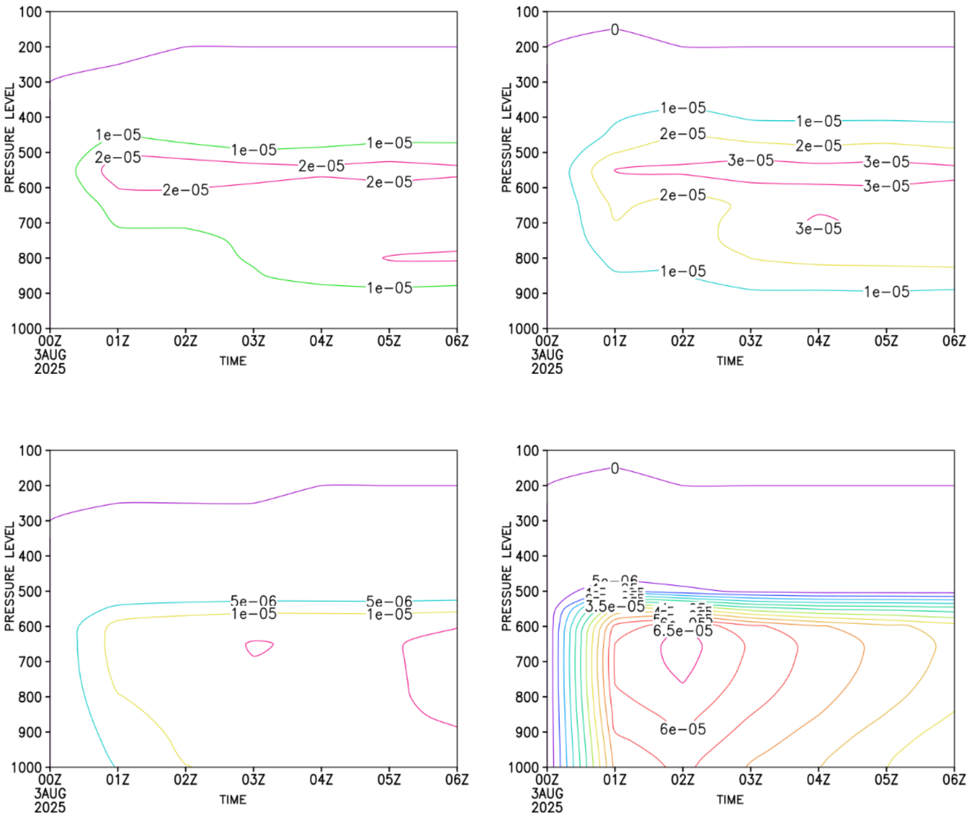

Figure 11. Vertical evolution of cloud water (top) and rainwater (bottom) over the main precipitation area (109°E–129°E, 22°N–32°N) during the first 6 hours of integration for ensemble member 1 initialized at 00:00 UTC on August 3, 2025 (Left: Control Forecast; Right: Cloud Analysis).

The vertical distribution of the temperature field in the cloud-free analysis experiment shows a monotonically decreasing trend with increasing altitude. Temperatures decrease from approximately 294 K near the surface (1000 hPa) to about 204 K in the upper atmosphere (100 hPa), consistent with the vertical temperature decrease characteristic of the troposphere. Temperature at the same altitude level changes gradually over time. For example, at 850 hPa, temperature slowly increases from 291 K to 294 K without significant fluctuations, reflecting the relatively stable evolution of the temperature field in the cloud-free analysis experiment. Regarding temperature differences between the cloud-containing and cloud-free analyses, high-value temperature differences are concentrated between 300 and 700 hPa (Mid-troposphere), with a maximum value of approximately 0.6 K, while differences near the surface (900–1000 hPa) and in the upper troposphere (100–200 h Pa)re smaller, ranging from 0 to 0.2 K. From a temporal evolution perspective, the mid-upper layer temperature difference peaks between 02Z and 04Z, gradually diminishing thereafter. This reflects that temperature adjustments introduced by cloud analysis are most pronounced during the early stages of precipitation system development. The positive temperature difference (cloud analysis temperature higher than no-cloud analysis temperature) indicates that the cloud analysis process elevates temperatures in the middle atmosphere (Figure 12). This phenomenon arises from latent heat release, i.e., vapor condensation (forming cloud water) and sublimation (forming ice) within cloud microphysical processes release substantial latent heat, leading to significant warming in the upper troposphere (e.g., 6–14 km) (Gorja et al., 2023). This constitutes the fundamental energy source driving convective development and sustaining warm-core structures. Cloud formation and maintenance are directly linked to latent heat release. When incorporating cloud information into cloud analysis processes, latent heat heating effects must be accounted for through coordinated adjustments to the initial temperature field to ensure thermodynamic equilibrium. During model integration, cloud radiative feedback primarily heats the atmosphere directly through longwave warming at the cloud base and shortwave absorption within clouds. It also induces large-scale, sustained dynamic warming in the middle and upper troposphere via the process of “cloud-top cooling → dynamic lifting → latent heat release.” This effect is not a direct consequence of cloud analysis itself, but rather a series of positive/negative feedback mechanisms automatically triggered by radiative transfer processes during subsequent model integration, once cloud analysis has successfully introduced a hydrometeor field with reasonable microphysical properties and spatial structure.

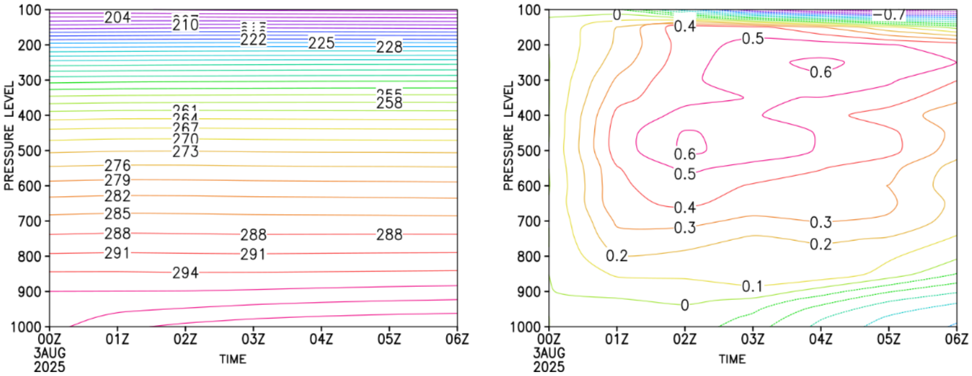

Figure 12. Vertical evolution of temperature of the first ensemble member over the main precipitation area (109°E–129°E, 22°N–32°N) during the first 6 hours of integration， initialized at 00:00 UTC on August 3, 2025. (left: Control Forecast; right: difference between cloud analysis experiment and control forecast).

From the vertical velocity profile of ensemble members(Figure 13), the cloud-free analysis vertical velocity field is nearly zero during the first few hours of model integration, with only weak ascent/descent observed in the lower levels (700–1000 hPa) over certain regions (e.g., 22°N–32°N).The cloud-free analysis reveals zones of strong upward motion: a broad area of vertical upward velocity (green/dark green regions) extends from the lower levels (900 hPa) to the upper levels (150 hPa) within the 22°N–32°N latitude band, with the maximum ascent velocity centered near 500–150 hPa. This ascent exhibits deep vertical continuity, indicating that cloud processes (such as latent heat release) drive intense systematic uplift. From the perspective of cloud analysis’s impact on atmospheric temperature fields, the condensation of water vapor within clouds releases substantial latent heat, directly heating the middle atmosphere. This reduces air parcel density, enhances buoyancy, and drives and sustains deep-seated upward motion. Consequently, the cloud analysis system significantly amplifies atmospheric vertical motion, particularly within the convectively active belt spanning 24°N–28°N. Here, latent heat release and cloud radiation feedback jointly drive deep-seated upward motion.

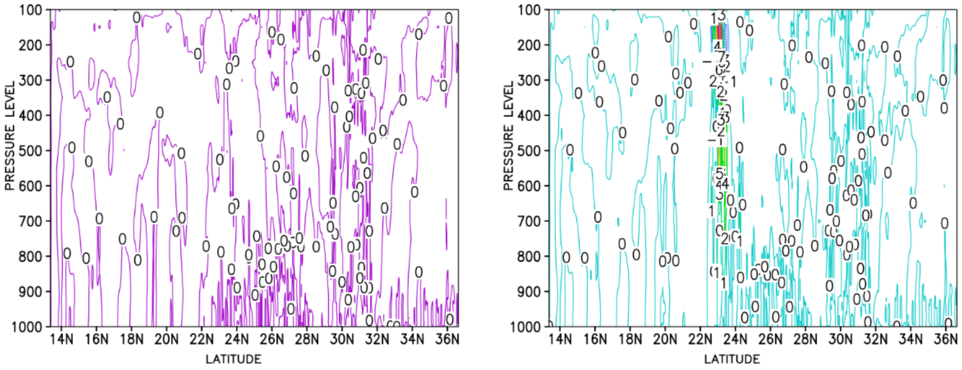

Figure 13. Vertical velocity along the 116°E meridional cross-section from the 1-hour model integration of ensemble member 1 initialized at 00:00 UTC on August 3, 2025 (Left: Control Forecast; Right: Cloud Analysis Experiment).

4.2. Impact of Cloud Analysis on Ensemble Uncertainty

To investigate the mechanism of remote sensing-driven cloud analysis in convective-scale ensemble forecasting, this study systematically evaluated its impact on ensemble forecasts of the 500 hPa geopotential height field, temperature field, and wind field U-component through comparative experiments with and without the assimilation of multi-source remote sensing data (three-dimensional mosaic radar reflectivity, hourly averaged FY-2G satellite TBB, and FY-2G total cloud water products). Statistical tests indicate that incorporating these radar and geostationary satellite observations via cloud analysis alters the initial perturbation structure and error growth dynamics of ensemble forecasts. This influence manifests as systematic improvements in forecast accuracy and reliability, rooted in the following interrelated physical mechanisms.

Statistical metrics of forecast performance show that experiments with remote sensing-based cloud analysis exhibit superior Continuous Rank Probability Scores (CRPS) across all forecast variables. Specifically, the CRPS values for experiments with assimilation of radar reflectivity and FY-2G cloud products were significantly lower than those without, with this advantage increasing as the forecast lead time extended from 12 to 48 hours. The most pronounced improvement was observed in the 500 hPa geopotential height field, followed by the temperature field, while the U-component wind field showed relatively moderate enhancement. This inter-variable discrepancy reveals the influence pathways of cloud processes on different physical quantities: errors in convective-scale forecasts primarily stem from moist convective processes. The physically coherent perturbations provided by remote sensing-derived cloud analysis target regions more likely to experience actual convection (as diagnosed from radar echoes and satellite TBB signatures), enabling efficient amplification along the core physical chain—“cloud water perturbation (from radar/satellite retrievals) → latent heat of phase change → thermal buoyancy → dynamic response.” This mechanism directly explains the reduction in CRPS: more accurate initial cloud and latent heat fields, directly constrained by observed radar reflectivity and FY-2G TBB/cloud water, enable the model to simulate convective heating processes more realistically from the integration start point, significantly reducing systematic biases in the potential height field (as the vertical integral of the thermal field) and temperature field. The improvement in wind fields, as a dynamic response variable, exhibits a smaller magnitude of improvement due to its relatively indirect position in the physical chain.

Regarding ensemble spread, the overall spread in the cloud-inclusive analysis experiment (which assimilates radar and satellite remote sensing data) was higher than in the cloud-exclusive experiment, particularly evident in the temperature and potential height fields. This shift indicates that the spatiotemporal variability and multiscale interactions inherent in cloud processes, as captured by remote sensing observations, introduce richer sources of uncertainty into the ensemble system. Consequently, the dispersion more closely approximates actual forecast errors, effectively mitigating the “insufficient dispersion” issue commonly observed in convective-scale ensemble forecasting. Notably, the improvement from remote sensing-based cloud analysis exhibits remarkable temporal stability: its enhancement of forecast accuracy and reliability persists across the 12- to 48-hour forecast lead time without diminishing with increasing integration time, demonstrating the sustained optimization capability of incorporating radar and satellite-derived cloud information into ensemble forecasting systems. Compared to traditional initial perturbation methods (e.g., ETKF), the cloud analysis system ingesting multi-source remote sensing data operates as an independent physical process for each ensemble member. It transforms minor background field differences between members into physically consistent, structured variations in hydrological fields such as cloud cover, cloud water, and precipitation particles, directly guided by observed radar reflectivity and FY-2G TBB/cloud water distributions. This introduces a perturbation source directly coupled with the model’s convective and microphysical processes into the ensemble system. Its high degree of physical coordination provides an essential foundation for the subsequent rational growth of perturbations.

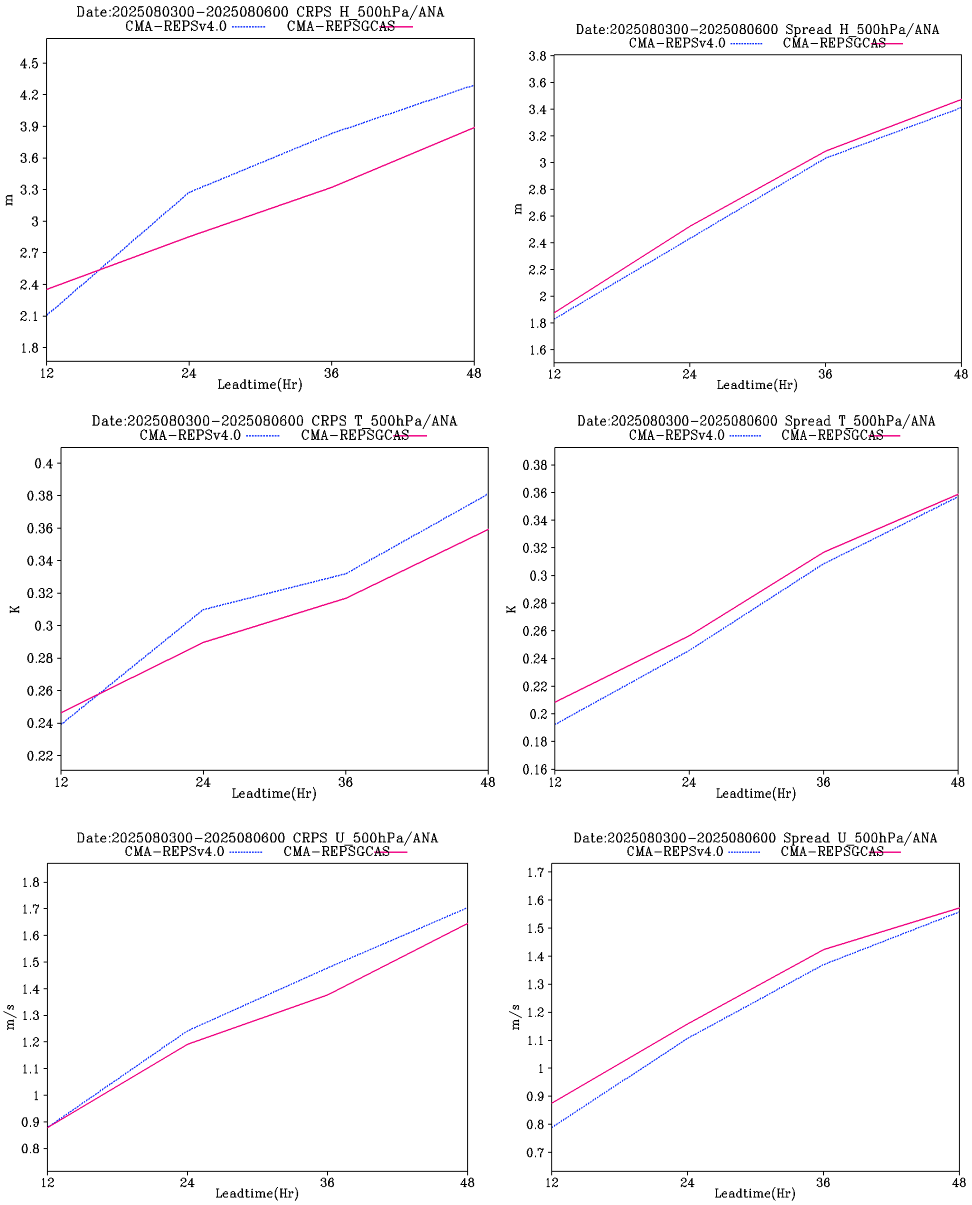

Figure 14. Evolution of 500 hPa geopotential height (top), temperature (middle), and wind field zonal component U CRPS (left) and SPREAD (right) with forecast lead time.

5. Conclusions and Outlook

Based upon traditional initial perturbations, this study independently runs a high-resolution cloud analysis system for each ensemble member, ingesting multi-source remote sensing data (three-dimensional mosaic radar reflectivity, hourly averaged FY-2G satellite black-body temperature (TBB), and FY-2G total cloud water products) to generate three-dimensional hydrometeor increment fields tailored to each member's atmospheric state. Through a Newtonian relaxation (nudging) scheme, these radar- and satellite-derived hydrometeor increments are progressively integrated into the model variables over the first few time steps to achieve smooth coordination between the hydrometeor field and the model's dynamic and thermal framework. Results indicate that:

(1) The nudging assimilation method avoids the potential disruption to the model's dynamic-microphysical equilibrium caused by a single large-scale injection of hydrometeors (which could trigger false intensification). Instead, the stepwise introduction of remote sensing-based hydrometeor fields allows the model to undergo a gradual adaptation and coordination process, better reflecting real physical evolution.

(2) The introduction of cloud processes derived from radar and FY-2G satellite observations significantly enhances the accuracy and reliability of convective-scale ensemble forecasts. Statistical tests reveal that for the geopotential height field, the cloud analysis system (which assimilates radar reflectivity and FY-2G TBB/cloud water) performs better at most lead times and levels, with the cloud-free analysis showing a slight edge only at the 500 hPa initial time (12h). For temperature fields, the cloud analysis system holds an overall advantage in mid-to-upper-level forecasts at 250 hPa and 500 hPa, with cloud-free analysis performing better only at the 850 hPa initial time. Regarding wind fields, the cloud analysis system notably improves the 850 hPa lower-level U and V components and the near-surface 10 m wind field, while differences in upper-level wind fields are insignificant. The near-surface 2 m temperature field also shows widespread improvement due to the introduction of remote sensing-driven cloud analysis. For precipitation forecasts, the cloud analysis system outperforms across all intensity levels, with particularly notable enhancements in heavy rain predictions. This maintains optimization effects while extending forecast lead times. This study provides crucial statistical evidence and physical basis, grounded in multi-source remote sensing data, for developing high-confidence convective-scale ensemble forecasting systems.

(3) An analysis of the physical mechanisms underlying the impact of cloud analysis on both individual ensemble members and the overall ensemble forecasting system indicates that assimilating radar and satellite remote sensing data primarily enhances ensemble forecasting performance through the following pathways:

First, the time required for the model to reach a certain precipitation intensity or cloud water content threshold shows that the cloud analysis scheme, directly constrained by observed radar reflectivity and FY-2G TBB/cloud water, significantly shortens the spin-up time, reducing the model's guessing process from water vapor to condensation and thereby establishing correct cloud-precipitation microphysical processes more rapidly.

Second, cloud analysis enables a more complete comprehensive characterization of the vertical distribution of cloud water and rainfall, allowing for more accurate simulation of cloud and precipitation formation processes. Changes in the humidity field play a fundamental role in numerical model precipitation forecasts; the input of realistic hydrometeor profiles from radar and satellite retrievals directly contributes to this improvement.

Third, the latent heat released from intra-cloud water vapor condensation directly heats the middle atmosphere, adjusting the thermal and dynamic structure at 500 hPa, thereby correcting forecast biases in geopotential height, temperature, and wind fields. This latent heat distribution is diagnosed from the ingested remote sensing data (e.g., radar reflectivity and satellite-derived cloud phase/top temperature).

Fourth, the complexity of cloud processes, as captured by high-resolution radar and geostationary satellite observations, provides ensemble members with initial perturbations closer to real atmospheric conditions, making dispersion better reflect actual forecast uncertainty and enhancing probabilistic forecasting reliability.

(4) Limitations and Future Prospects: The introduction of cloud analysis schemes into convective-scale ensemble forecasting systems significantly enhances the overall forecasting capability of cloud-resolving ensemble systems. However, cloud analysis quality remains highly dependent on the coverage and quality of remote sensing observations from radars, satellites, and other sources(e.g., the three-dimensional mosaic radar reflectivity, FY-2G hourly TBB, and total cloud water products used in this study). While the cloud analysis scheme offers computational efficiency and ease of implementation within the operational ensemble framework, compared to variational assimilation methods in incorporating hydrometeor control variables, it falls short in the synergistic

optimization of hydrometeors and the dynamic field. Developing superior analytical assimilation schemes that more effectively leverage multi-source remote sensing data represents the future direction for regional ensemble forecasting within the CMA.

In summary, incorporating cloud analysis processes into regional convective-scale ensemble forecasting systems represents a key technological approach to addressing the spin-up challenge in model forecasting by tackling it at its source—the initialization stage. By assimilating high-resolution radar and FY-2G satellite observations, this method integrates physically consistent cloud and precipitation information into ensemble members through coordinated thermal, dynamic, and microphysical adjustment, delivering thermally, dynamically, and microphysically consistent thermally-started initial fields. Consequently, it significantly enhances the performance of numerical models, particularly in short-term ensemble forecasting.

Author Contributions: Conceptualization and methodology, Xiefei Zhi, Guo Deng and Lijuan Zhu; Mechanism Diagnosis of Cloud Analysis Impact, Yushu Zhou and Xiefei Zhi; ensemble verification, Fajing Chen and Kaiyuan Wu; Cloud resolving ensemble system software: Jing Chen, Hongqi Li,Jingzhuo Wang,Guo Deng, Jian Yue and Zhizhen Xu; Writing: Guo Deng, Xiefei Zhi,Lijuan Zhu andYushu Zhou. All authors have read and agreed to the published version of the manuscript.

Funding: This research was jointly funded by the Guidance Project for Science and Technology Plan of Fujian Province (Grant 2024Y0076), the National Natural Science Foundation of China (NSFC) Projects (Grant Nos. 42475169, 42175012, 41975137), and the Science and Technology Winter Olympics Special Subject (Grant No. 2018YFF0300103).

Data Availability Statement: The data presented in this study are available on request from the corresponding author and first author. The original data presented in the study are openly available in Zenodo at https://doi.org/10.5281/zenodo.18335391.

Data Availability Statement: We encourage all authors of articles published in MDPI journals to share their research data. In this section, please provide details regarding where data supporting reported results can be found, including links to publicly archived datasets analyzed or generated during the study. Where no new data were created, or where data is unavailable due to privacy or ethical restrictions, a statement is still required. Suggested Data Availability Statements are available in section “MDPI Research Data Policies” at https://www.mdpi.com/ethics.

Acknowledgments: All datasets except Radar data used in this study—including FY-2G satellite black-body temperature (TBB), FY-2G total cloud water products, and ensemble experiments data—are publicly available. The FY-2G datasets can be downloaded from the National Satellite Meteorological Center of China (NSMC) website: http://satellite.nsmc.org.cn/portalsite/default.aspx?currentculture=en-US. The ensemble experiments data are available from https://pan.baidu.com/s/4svuwnFn.

Acknowledgments: Data All datasets used in this study—including FY-4A/GIIRS, the cloud mask product of FY-4A/AGRI, and FNL reanalysis data—are publicly available. The FY-4A/GIIRS, and cloud mask of FY-4A/AGRI datasets can be downloaded from the National Satellite Meteorological Center of China (NSMC) website: http://satellite.nsmc.org.cn/portalsite/default.aspx?currentculture=en-US. The two convective-scale ensemble forecast experiments (without and with cloud analysis) data: https://pan.baidu.com/s/4iGNsNtV.

Conflicts of Interest: The authors declare no conflicts of interest.

References

Albers, S.C.; McGinley, J.A.; Birkenheuer, D.L.; Smart, J.R. The Local Analysis and Prediction System (LAPS): Analyses of clouds, precipitation, and temperature.Weather Forecast.1996,11(3), 273–287.

Bauer, P.; Lopez, P.; Benedetti, A.; Salmond, D.; Moreau, E. Implementation of 1D+4D-Var assimilation of precipitation-affected microwave radiances at ECMWF. Part II: 4D-Var.Q. J. R. Meteorol. Soc.2007,132, 2307–2332.

doi:10.20944/preprints202605.1096.v1

Bei, N.; Zhang, F. Impacts of initial condition errors on mesoscale predictability of heavy precipitation along the Mei-Yu front of China.Q. J. R. Meteorol. Soc.2007,133, 83–99.

Benjamin, S.G.; Weygandt, S.S.; Brown, J.M.; Hu, M.; Alexander, C.R.; Smirnova, T.G.; Olson, J.B.; James, E.P.; Dowell, D.C.; Grell, G.A.; et al. A North American Hourly Assimilation and Model Forecast Cycle: The Rapid Refresh. Mon. Wea. Rev.2016,144(4), 1669–1694. Doi:https://doi.org/10.1175/MWR-D-15-0242.1.

Brewster, K. Application of a Bratserth analysis scheme including Doppler radar data. In Proceedings of the 15th Conference on Weather Analysis and Forecasting, Norfolk, VA, USA, 19–23 August 1996; American Meteorological Society: Boston, MA, USA, 1996; pp. 92–95.

Chen, J.; Zhu, Y.J.; Duan, W.S.; et al. A review on development, challenges, and future perspectives of ensemble forecast.J. Meteor. Res.2025,39(3), 534–558. doi:10.1007/s13351-025-4909-4.

Denis, B.; Côté, J.; Laprise, R. Spectral decomposition of two-dimensional atmospheric fields on limited-area domains using the discrete cosine transform (DCT).Mon. Wea. Rev.2002,130(7), 1812–1829. DOI:https://doi.org/10.1175/1520-0493(2002)130<1812:SDOTDA>2.0.CO;2.

Destouches, M.; Montmerle, T.; Michel, Y.; Caron, J.-F. Impact of hydrometeor control variables in a convective-scale 3DEnVar data assimilation scheme.Q. J. R. Meteorol. Soc.2023,149(752), 757–780. DOI:https://doi.org/10.1002/qj.4426.

Duda, J.D.; Wang, X.; Wang, Y.; Carley, J.R. Comparing the Assimilation of Radar Reflectivity Using the Direct GSI-Based Ensemble–Variational (EnVar) and Indirect Cloud Analysis Methods in Convection-Allowing Forecasts over the Continental United States.Mon. Wea. Rev.2019,147(5), 1655–1678. DOI:https://doi.org/10.1175/MWR-D-18-0171.1.

Gorja, M.M.K.; Challa, V.S.; Viswanadhapalli, Y.; Vissa, N.K.; Balasubramanian, V. *Sensitivity of cloud microphysics on the simulation of heavy rainfall in WRF-a case study for the 7-10 August 2019 event over Kerala, India.Atmos. Res.2023,288, 106715. DOI:10.1016/j.atmosres.2023.106715.*

Hohenegger, C.; Schär, C. Atmospheric predictability at synoptic versus cloud-resolving scales.Bull. Am. Meteorol. Soc.2007,88(11), 1783–1793. DOI:https://doi.org/10.1175/BAMS-88-11-1783.

Hohenegger, C.; Schär, C. Predictability and error growth dynamics in cloud-resolving models.J. Atmos. Sci.2007,64(12), 4467–4478. DOI:https://doi.org/10.1175/2007JAS2143.1.

Hu, M.; Xue, M.; Brewster, K. 3DVAR and cloud analysis with WSR-88D level-II data for the prediction of the Fort Worth, Texas, tornadic thunderstorms. Part I: Cloud analysis and its impact. Mon. Wea. Rev.2006,134(2), 675–698. DOI:https://doi.org/10.1175/MWR3092.1.

Jiang, R.; Wang, Y.; Xie, J.; Zhao, Y.; Li, F.; Wang, X. Assessment of extreme precipitation events and their teleconnections to El Niño Southern Oscillation, a case study in the Wei River Basin of China.Atmos. Res.2019,218, 372–384.https://doi.org/10.1016/j.atmosres.2018.12.015.

Johnson, M.; Snook, N.; Park, J.; Xue, M.; Brewster, K.A.; Supinie, T.; Hu, X.-M. Severe weather verification of an FV3-LAM regional ensemble during the 2022 NOAA Hazardous Weather Testbed Spring Forecasting Experiment. Weather Forecast.2025,40(4), 577–592. DOI:https://doi.org/10.1175/WAF-D-24-0034.1.

Koch, S.E.; Aksakal, A.; McQueen, J.T. The influence of mesoscale humidity and evapotranspiration fields on a model forecast of a cold-frontal squall line.Mon. Wea. Rev.1997,125(3), 384–409. DOI:https://doi.org/10.1175/1520-0493(1997)125<0384:TIOMHA>2.0.CO;2.

Liu, X.; Chen, J.; Liu, Y.; et al. An Initial Perturbation Method for the Multiscale Singular Vector in Global Ensemble Prediction.Adv. Atmos. Sci.2024,41, 545–563. https://doi.org/10.1007/s00376-023-3035-4.

Pan, Y.; Xue, M.; Ge, G. Incorporating diagnosed intercept parameters and the graupel category within the ARPS cloud analysis system for the initialization of double-moment microphysics with the assimilation of reflectivity data and testing with a squall line over south China.Mon. Wea. Rev.2016,144(1), 371–392. DOI:https://doi.org/10.1175/MWR-D-15-0008.1.

Pan, Y.; Xue, M. Impacts of humidity adjustment through radar data assimilation using cloud analysis on the analysis and prediction of a squall line in southern China.Earth Space Sci.2020,7(3), e2019EA000893. https://doi.org/10.1029/2019EA000893.

Phillips, N.A. On the problem of initial data for the primitive equations.Tellus1960,12(2), 121–126. DOI:https://doi.org/10.1111/j.2153-3490.1960.tb01289.x

Smith, R.N.B. A scheme for predicting layer clouds and their water content in a general circulation model.Q. J. R. Meteorol. Soc.1990,116(492), 435–460. .https://doi.org/10.1002/qj.49711649210.

Stensrud, D.J.; Xue, M.; Wicker, L.J.; Kelleher, K.E.; Foster, M.P.; Schaefer, J.T.; Schneider, R.S.; Benjamin, S.G.; Weygandt, S.S.; Ferree, J.T.; Tuell, J.P. Convective-Scale Warn-on-Forecast System: A Vision for 2020.Bull. Am. Meteorol. Soc.2009,90(10), 1487–1499. DOI:https://doi.org/10.1175/2009BAMS2795.1.

Sun, J.; Crook, N.A. Dynamical and microphysical retrieval from Doppler radar observations using a cloud model and its adjoint. Part I: Model development and simulated data experiments.J. Atmos. Sci.1997,54(12), 1642–1661. DOI:https://doi.org/10.1175/1520-0469(1997)054<1642:DAMRFD>2.0.CO;2.

Toth,Z.,and E.Kalnay,Ensemble forecasting at NMC: The generation of perturbations. Bull. Amer. Meteor. Soc.,1993,74, 2317–2330,https://doi.org/10.1175/1520-0477(1993)0742.0.CO;2.

Wang, H.; Liu, Y.; Duan, J.; Shi, Y.; Lou, X.; Li, J. Assimilation of radar reflectivity using a time-lagged ensemble based ensemble Kalman filter with the "cloud-dependent" background error covariances.J. Geophys. Res. Atmos.2022,127(10), e2021JD036207. https://doi.org/10.1029/2021JD036207.

Wallace, J. M., and P. V. Hobbs, 2006:Atmospheric Science: An Introductory Survey(2nd ed.). Academic Press. https://doi.org/10.1016/C2009-0-00034-8.PP504.

Wang,X.G.,andC.H.Bishop, A comparison of breeding and ensemble transform Kalman filter ensemble forecast schemes. 2003,J. Atmos. Sci., 60, 1140–1158, https://doi.org/10. 1175/1520-0469(2003)0602.0.CO;2.

Wilson, J.W.; Roberts, R.D. Summary of convective storm initiation and evolution during IHOP: Observational and modeling perspective. Mon. Weather Rev.2006,134(1), 23–47. DOI:https://doi.org/10.1175/MWR3069.1

Xue, J.S.; Chen, D.H.Scientific Design and Applications of the GRAPES Numerical Prediction System; Science Press: Beijing, China, 2008; p. 383. (In Chinese)

Xue, M.; Hu, M.; Schenkman, A. Numerical prediction of 8 May 2003 Oklahoma City tornadic supercell and embedded tornado using ARPS with assimilation of WSR-88D radar data.Wea Forecasting.2014,29(1), 39–62. DOI:https://doi.org/10.1175/WAF-D-13-00029.1.

Xue, M.; Wang, D.-H.; Gao, J.-D.; Brewster, K.; Droegemeier, K.K. The Advanced Regional Prediction System (ARPS), storm-scale numerical weather prediction and data assimilation. Meteorol. Atmos. Phys.2003,82(1), 139–170. DOI:10.1007/s00703-001-0595-6.

Zhang, F.; Carr, F.; Brewster, K. ADAS cloud analysis. In Proceedings of the 12th Conference on Numerical Weather Prediction, Phoenix, AZ, USA, 11–16 January 1998; American Meteorological Society: Boston, MA, USA, 1998; pp. 185–188.

Zhang, H.; Chen, J.; Zhi, X.; Wang, Y.; Wang, Y. Study on multi-scale blending initial condition perturbations for a regional ensemble prediction system.Adv. Atmos. Sci.2015,32(8), 1143–1155. DOI:https://doi.org/10.1007/s00376-015-4232-6.

Zhang, J.Moisture and diabatic initialization based on radar and satellite observations; Ph.D. Dissertation, University of Oklahoma, Norman, OK, USA, 1999; p. 203.

Zhang, X. Application of a convection-permitting ensemble prediction system to quantitative precipitation forecasts over southern China: Preliminary results during SCMREX. Q. J. R. Meteorol. Soc.2018,144(717), 2842–2862. DOI:https://doi.org/10.1002/qj.3411.

Zhang, X.; Min, J.; Wu, T. A study of ensemble-sensitivity-based initial condition perturbation methods.Atmos. Res. 2020,234, 104741.DOI:https://doi.org/10.1016/j.atmosres.2019.104741.

Zhao, K.; Xue, M. Assimilation of coastal Doppler radar data with the ARPS 3DVAR and cloud analysis for the prediction of Hurricane Ike (2008).Geophys. Res. Lett.2009,36(12), L12803. https://doi.org/10.1029/2009GL038658.

Zhou, K.H.; Zheng, Y.G.; Yang, B.; et al. Objective nowcasting of severe convective weather: Technological progress and outlook.J. Meteor. Res.2025,39(3), 724–740. DOI:https://doi.org/10.1007/s13351-025-4907 6. DOI:https://doi.org/10.1016/j.atmosres.2022.106101.

Zhu, L.; Kang, W.; Li, W.; Luo, J.J.; Zhu, Y. The optimal bias correction for daily extreme precipitation indices over the Yangtze-Huaihe River Basin, insight from BCC-CSM1.1-m.Atmos. Res.2022,271, 106101. DOI:https://doi.org/10.1016/j.atmosres.2022.106101.

doi:10.20944/preprints202605.1096.v1

Zhu, L.J.; Gong, J.D.; Huang, L.P.; et al. Three-dimensional cloud initial field created and applied to GRAPES numerical weather prediction nowcasting.J. Appl. Meteor. Sci.2017,28(1), 38–51. DOI:10.11898/1001-7313.20170104 (In Chinese)